The Shuram excursion: A response to climate extremes at the dawn of animal life

Kristin Bergmann[1,1], Magdalena R Osburn[2,2], Julia Wilcots[1,1], Marjorie Cantine[1,1], John P Grotzinger[3], Woodward W Fischer[3,3], John M Eiler[3], Magali Bonifacie[4,4], and Nicholas Boekelheide[1]

[1]Massachusetts Institute of Technology
[2]Northwestern University Evanston
[3]California Institute of Technology
[4]Institut de Physique du Globe Paris

November 30, 2022

Abstract

The Ediacaran-aged Shuram excursion was the last and largest of the Neoproterozoic negative carbon isotope anomalies. Recognized in stratigraphic successions around the globe, it precedes diverse evidence for macroscopic, multicellular life, and follows the Cryogenian global glaciations and Ediacaran Gaskiers glaciation. Hypotheses for the cause of the Shuram excursion can be broadly grouped into those that argue for post-depositional diagenetic alteration of the carbon isotope record and those that argue the extremely low δ13C values reflect a primary perturbation to the carbon cycle. Given the timing and magnitude of this event, distinguishing between these disparate hypotheses, or combining them, is critical for reconstructing the environmental conditions under which complex life evolved on Earth. We test specific predictions of each model using a range of stratigraphic observations and micro- and macro-analytical techniques. We find that the type sections in Oman where the Shuram excursion was first described are well preserved and contain a range of features difficult to reconcile with a post-depositional origin. However, many salient features are consistent with an extreme warming event coupled to a carbon cycle perturbation, analogous to the Paleocene-Eocene Thermal Maximum (PETM), and increased middle Ediacaran volcanism. We propose that cooling associated with the recovery was critical for origination rates of macroscopic soft-bodied organisms.

Title:
The Shuram excursion: A response to climate extremes at the dawn of animal life

Kristin D. Bergmann[1*], Magdalena R. Osburn[2], Julia Wilcots[1,3], Marjorie D. Cantine[1,4], Nicholas Boekelheide[1], Woodward W. Fischer[5], Magali Bonifacie[6]

[1]Department of Earth, Atmospheric and Planetary Sciences,
Massachusetts Institute of Technology,
Cambridge, MA 02139
[2]Department of Earth and Planetary Sciences, Northwestern University
Evanston, IL 60208
[3]now at Department of Geosciences, Princeton University
Princeton, New Jersey
[4]now at Institut für Geowissenschaften, Goethe-Universität Frankfurt
Frankfurt, Germany
[5]Division of Geological and Planetary Sciences, California Institute of Technology
Pasadena, CA 91125
[6]Institut de Physique du Globe de Paris, Université Paris Cité
1 Rue Jussieu, 75005 Paris, France
*To whom correspondence should be addressed; E-mail: kdberg@mit.edu.

The Ediacaran-aged Shuram excursion was the last and largest of the Neoproterozoic negative carbon isotope anomalies. Recognized in stratigraphic successions around the globe, it precedes diverse evidence for macroscopic,

multicellular life, and follows the Cryogenian global glaciations and Ediacaran Gaskiers glaciation. Hypotheses for the cause of the Shuram excursion can be broadly grouped into those that argue for post-depositional diagenetic alteration of the carbon isotope record (*1–7*) and those that argue the extremely low δ^{13}C values reflect a primary perturbation to the carbon cycle (*8–10*). Given the timing and magnitude of this event, evaluating these disparate hypotheses is critical for reconstructing the environmental conditions under which complex life evolved on Earth. We test specific predictions of each model using a range of stratigraphic observations and micro- and macro-analytical techniques. We find that the type sections in Oman where the Shuram excursion was first described are well-preserved and contain a range of features difficult to reconcile with a post-depositional origin. Many salient features of these sections, however, can be well-explained by an extreme warming event coupled to a carbon cycle perturbation, analogous to the Paleocene-Eocene Thermal Maximum (PETM), and increased middle Ediacaran volcanism. We propose that both mass extinction and the diversification of Ediacaran eukaryotes, including animals, were driven by temperature changes across the Shuram excursion.

One sentence summary: Macro- and micro-scale sedimentological and geochemical observations of Earth's largest negative carbon excursion support its interpretation as an extreme hyperthermal event.

Main Text: Neoproterozoic sedimentary successions record a series of pronounced negative carbon isotope excursions. The most extreme of these, the Ediacaran-aged Shuram carbon isotope excursion (CIE), drops from baseline $\delta^{13}C_{VPDB}$ values of +5‰ to as low as 12‰ within

tens of meters of vertical stratigraphic section, and then gradually recovers to +5‰ often over several hundred meters, in multiple sections globally (*11*). The Shuram excursion has been hypothesized to result either from secondary (diagenetic) processes that postdate deposition (*1–7*) or from primary changes in water column dissolved inorganic carbon (DIC) (*8, 9, 12*).

Arguments for a diagenetic origin for the Shuram excursion include: the extreme magnitude of negative values in the nadir, beyond mantle input values which challenge traditional global carbon isotope budget models (*1, 13*); high Mn/Sr and Fe/Ca ratios in the excursion nadir (*3*); and the association of low δ^{13}C values with anomalously low δ^{18}O values—geochemical features often interpreted as signatures of carbonate diagenesis (*2, 3, 11*). It has been suggested that diagenesis could have produced the Shuram excursion either by flushing large volumes of ^{13}C-poor fluids through carbonate rocks (fluid-buffered alteration) either early or late in the burial history (*2, 3, 6*) or by the authigenic precipitation of cements and other secondary carbonates from pore fluids with low δ^{13}C values driven by microbial processes associated with organic diagenesis (sediment-buffered alteration) (*1, 7, 14*). Additional models based on Ca isotopic pattens suggest that some stratigraphic intervals of the stratigraphy experienced sediment-buffered alteration while others experienced fluid-buffered alteration (*4, 5, 15*). Each diagenetic model makes specific predictions for the characteristics of rocks recording the excursion, including the petrographic phases present; their geochemical variability at small spatial scales; the temperatures they record in carbonate clumped isotopes; and the composition of the fluid from which they precipitated (*16*)(Table 1).

A primary origin for the Shuram excursion is supported by the wide paleogeographic occurrence of middle Ediacaran negative CIEs. Concurrent Re/Os ages from the CIEs in Oman and NW Canada also suggest the Shuram excursion is a primary carbon cycle perturbation with a shorter duration than previously suggested (*17*). Five locations (Oman, NW Canada, Australia,

Peru, and Southern California) have similar isotopic (C, O, Ca, Sr) and bulk elemental patterns (Mn, Sr, Mg) (*15*). When viewed as a whole, the geochemical data preserve clear trends associated with a primary depositional depth gradient (*15*). Stratigraphy in Australia preserve depleted clasts in breccias deposited soon after the excursion nadir (*18*). High resolution δ^{13}C trends preserve evidence of a landward transgression of an ooid grainstone in Southern California (*19*). Five other locations also demonstrate a clear association between the onset of the excursion and sea level rise (*15, 20*). These locations have other sedimentological features in common including climbing wave ripples and storm deposits including edgewise conglomerates (*15, 21–23*).

In the Phanerozoic, there is a widely recognized relationship between climate change and many CIEs identified globally (*24–26*), in part expressed as co-variation in δ^{13}C and δ^{18}O, a key feature of the Shuram Excursion. Coupled climate and carbon cycle perturbations like the Paleocene-Eocene thermal maximum (PETM) are recorded in a wide range of sedimentologic and isotopic datasets. During the PETM, a CO_2 or methane-driven temperature increase is recorded by multiple proxies including Mg/Ca ratios of foraminifera and carbonate clumped-isotope temperature change in marine and terrestrial environments (*27, 28*). Physical consequences of warming include the thermal expansion of seawater and subsequent sea level rise, as well as a flashy hydrologic cycle characterized by severe and frequent storms (*29, 30*). Many deep-sea cores show a characteristic red clay interval associated with the PETM event horizon in otherwise carbonate-rich strata which has been interpreted as a sedimentological expression of carbonate dissolution following ocean acidification and a shoaling of the carbonate compensation depth (CCD) (*31*). Shallow water environments document a smaller magnitude pH change. Both deep and shallow oceans contribute CO_2 release to the atmosphere (*32*). Anoxia and expanded oxygen minimum zones, in part due to temperature-dependent O_2 solubility, can

be tracked with a variety of proxies including biomarkers and I/Ca (*33, 34*). An initial period of rapid physical weathering in a hot and arid climate with minimal chemical breakdown is represented by sands and micaceous silts at multiple localities (*35*). A transition to a warm and wet climate led to significant chemical weathering and deposition of kaolinites (*36*) and geochemical proxy evidence for enhanced weathering (i.e. $^{187}Os/^{188}Os$) (*37*). Biologic consequences from warming, anoxia, and ocean acidification include extinction, migration and origination in both terrestrial and marine fossil records (*38*).

Different hypotheses for the driving mechanism of the Shuram excursion make distinct predictions that can be evaluated using the rock record (Table 1). We evaluate predictions from each diagenetic model using sedimentology and stratigraphy, petrography, mineralogy, a range of micro-and macro-analyses of trace element and isotopic variability, and carbonate clumped isotope thermometry. We compare these results with observations of the PETM, a Phanerozoic hyperthermal, to argue that the Shuram represents a similar, though more extreme, event. We also compile known volcanic occurrences within the age range of the Shuram excursion (*17*) and identify a potential driver for climate change. If a primary coupled climate-carbon cycle perturbation model unifies the range of observations associated with Shuram excursion-hosting strata worldwide, the magnitude of $\delta^{18}O$ change predicts this is one of the most extreme surface ocean warming events in the last 600 million years.

Results and Discussion To test predictions from post-depositional diagenetic and primary models for the Shuram excursion, two stratigraphic sections were studied from shallowly buried strata in the Huqf outcrop area (Mukhaibah Dome (MD) & Khufai Dome (KD), < 2 km max burial depth) (*16, 39*). The two sites preserve a range of shallow marine depositional environments through time.

Sedimentology and Stratigraphy Detailed lithofacies and sequence stratigraphic analysis allows us to assess the sedimentological and stratigraphic predictions of each proposed mechanism against the rock record (Table 1). The Shuram excursion in Oman is recorded in the strata of the Khufai, Shuram and Buah formations within the Ediacaran- to Cambrian-aged Huqf Supergroup (*20, 40, 41*)(Fig. S1). In the Huqf Outcrop Area, the pre-excursion strata of the Khufai Formation transition from deep-water calcitic mudstone and wackstone lithofacies to shallow water dolomitic tepees, stromatolites, and edgewise conglomerates consistent with a peritidal and shallow subtidal depositional environment (*20*)(Fig. 1A,E). The onset of the Shuram excursion coincides with sea level rise recorded in a transgressive dolomitic oolite, stromatolite, and mudstone lithofacies of the uppermost Khufai Formation ($\delta^{13}C_{VPDB}$ of 1 to 5.3‰)(Fig. 1B,F) (*20, 42*). The nadir of the excursion ($\delta^{13}C_{VPDB}$ of 8 to 12‰) is recorded in subtidal, cross-stratified, calcitic ooid grainstones and edgewise conglomerates, that are intercalated with hummocky cross-stratified, red, micaceous, siliciclastic siltstones in the Shuram Formation (*41*))(Fig. 1C,G). The recovery of the excursion ($\delta^{13}C_{VPDB}$ values of 8 to +2‰) occurs in a thick limestone succession ($\sim$200 m) of subtidal crinkly laminated mudstone, edgewise conglomerates and large meter-scale domal stromatolites of the Buah Formation (*43*)(Fig. 1D,H). A sequence boundary occurs near the contact between the Shuram Formation and Buah Formation as evidenced by increased sand, lenticular to wavy lamination, and evaporite mineral laths. As a whole, the lithofacies in the nadir and recovery of the Shuram excursion suggest storm-dominated conditions (Fig. 1). Climbing ripples and and loading structures including ball and pillow structures from dewatering indicate rapid sedimentation during the nadir.

Petrography To evaluate the predictions from sediment- and fluid-buffered diagenesis in carbonate microfacies (Table 1), we examined petrographic thin sections from throughout the excursion. Well below the onset of the excursion, the lower Khufai Formation has coarsely crys-

talline fabrics, evidence of dissolution and veining in the calcitic deep water mudstones and wackstones (Fig. 2F, Fig. S1). However, the carbonates from just below, in the Shuram excursion, and after it preserve small crystal sizes of micrite and microspar in mudstones, and ooids with optically oriented, radial crystal fabrics (*16, 20, 44*)(Fig. 2A-E).

Ooids—spherical carbonate grains that form in shallow water environments—are particularly useful in evaluating alteration processes because these grains precipitate directly from seawater and, if primary fabrics are preserved, distinct crystal patterns are observable. There are two separate oolitic intervals capturing the Shuram excursion. One bed, 5–20 m thick, at the top Khufai Formation captures the onset of the excursion ($\delta^{13}C_{VPDB}$values of 0 to 5‰)(Fig. 1B,F,2B). This bed also includes mudstone rip-up clasts and micritic stromatolites that nucleated on the grainstone and generated synoptic topography above the oolite(Fig. 1C). The second oolitic interval is in the nadir of the excursion ($\delta^{13}C_{VPDB}$values of 9 to 12‰). Oolite beds are interbedded with siltstones spanning a 100 m interval in the Shuram Formation(Fig. 1C,2D,E).

We utilized petrography, EBSD, and SEM to quantify crystal sizes and orientations of ooid fabrics from the onset and nadir of the excursion. The dolomite ooids from the onset of the excursion preserve a radial, plumose fabric composed of fine crystals as seen in nano-scale synchrotron-based PIC mapping and EBSD (*16, 20, 44*)(Fig. 3A,B). The ooids are often silica-cemented or silicified, particularly in the northern Huqf outcrop area (*16, 20, 44*)(Fig. 2B). In SEM after cryo-fracturing, there is also significant authigenic Mg silicate clay present, likely palygorskite because of its minor Al and microfibrous fabric (Fig. 3E,F). The dolomite crystals often appear to template on the palygoskite on the outer rind of the nucleus and in the cortex, replicating the curved shapes and interlocking, fibrous matted textures (Fig. 3C,F).

The calcitic ooid grainstones from the nadir of the excursion ($\delta^{13}C_{VPDB}$values of -8 to $-12‰$) in the Shuram Formation are often trough cross-stratified, and in thin section contain alternating siliciclastic and cement-rich horizons that infill around the ooids (Fig. 1C, 2D,E). These ooids also have a radial fabric and are composed of elongate crystals that do not display micritization or equant-mosaic replacement texture. Electron backscatter diffraction (EBSD) demonstrates the radial crystals within the calcite ooids are oriented with the c-axis parallel to growth direction (Fig. 3G,H,I). Pore-filling cements can inherit the orientation of the nearest ooid crystal, but in general are blocky and randomly oriented. The radial calcite crystals are larger, more planar, and always length-fast compare to the dolomite crystals in Fig. 3A and B.

Mineralogy To better characterize the mineralogy of the carbonates hosting the Shuram excursion, and to determine whether variability represents selective alteration of primary aragonite (*4*), or some other process, we used XRD, electron backscatter detection (EBSD), electron microprobe elemental mapping and spot analysis, and strong- and weak-acid bulk-dissolutions using inductively coupled atomic emission spectrometry.

The dolomite facies of the Upper Khufai Formation are ordered, stoichiometric dolomite today, including the transgressive oolite described above with co-associated Mg silicate clays and silica cements. Together the crystal structure and mineral co-associations provide good evidence these dolomite ooids formed as primary dolomite (*44*). Combined this could suggest alkaline conditions with high activities of Si and Mg, which may have aided in primary dolomite formation (*45*).

A stratigraphically coherent mineralogical change from dolomite to limestone at the boundary with the Shuram Formation is confirmed with both x-ray diffraction (XRD) and bulk trace metal data. Electron microprobe spot analyses of individual calcitic ooids in the nadir of the

Shuram excursion indicate low Mg and Sr concentrations (Mg: mean 0.44 ± 0.01%, Sr: 124 ± 29 ppm, Fe: 1712 ± 133 ppm, Mn: 815 ± 48 ppm, ± 1 S.E.)(Table S1), and, along with the radial ooid fabric observed in Fig. 3G,H,I, further support a primary calcite mineralogy for this interval.

In contrast, EPMA spot analyses in the stratigraphy that records the recovery from the Shuram excursion can have Sr concentrations as high as 1596 ppm ± 29 ppm, indicating this interval might have been primary aragonite prior to dissolution and calcite replacement. Despite this process, the mudstones, edgewise conglomerates, and crinkly laminites are still micrite and microspar, thus the transformation likely occurred under sediment-buffered conditions.

The macro-scale observations of mineralogical changes are common across many Shuram excursion-bearing successions (*15, 19*). Our results, while surprising, suggest this is best understood as changing conditions in shallow marine enviroments to promote primary dolomite precipitation in the excursion onset, primary calcite precipitation in the nadir, and finally primary aragonite precipitation in the recovery.

Trace elements Some hypotheses suggest that high concentrations of Fe and Mn measured from bulk dissolution of rocks from the nadir of the excursion reflect the addition of Fe^{+2} and Mn^{+2} from reduced fluids during diagenesis (*1, 3*)(Fig. S2). We tested these hypotheses using three methods: 1. electron microprobe (EPMA) elemental mapping and spot analysis, 2. comparisons between analyses of strong- and weak-acid bulk-dissolutions using inductively coupled atomic emission spectrometry, and 3. synchrotron x-ray absorption near-edge spectroscopy (XANES).

EPMA maps of Fe and Mn show spatial variability, not homogeneously distributed elemental enrichment associated with dissolution and reprecipitation in low oxygen pore fluids (Fig. 4). High iron concentration in EPMA spot analyses within ooids can be attributed to ultrafine inclusions of hematite, likely detrital in origin ($<$1 μm)(Fig. 4I, Fig. S5, S6). Some authigenic hematite coating detrital grains and mineralized ooids along surfaces likely represents mineralization during depositional hiatuses(Fig. 4I, Fig. S5). These surfaces are often capped by intervals lean in detrital sediments but rich in secondary cement, indicating faster ooid deposition. XANES analyses indicate that iron is present primarily as Fe(III) in hematite and mixed valence in biotite (Fig. S4).

The high bulk Mn contents of the oolitic grainstones (up to 3670 ppm) exceeds those of the individual ooids (mean 815 ± 48 ppm, ± 1 S.E.) and can be attributed to manganese-rich pink cements (Mg: mean 0.37 ± 0.02%, Sr: 0 ppm, Fe: 647 ± 165 ppm, Mn: 7853 ± 587 ppm, ± 1 S.E.), which fill interstices between ooids (Fig. 4O, Fig. S6). These pink cements constitute a diagenetic fabric, and confirm that the high Mn contents of Shuram rocks are a result of post-depositional processes. However, these pink cements pre-date a second, porosity-occluding, sparry calcite cement (Mg: mean 0.33 ± 0.02%, Sr: 141 ± 37 ppm, Fe: 912 ± 109 ppm, Mn: 1532 ± 106 ppm, ± 1 S.E.) indicating they formed during early diagenesis in the shallow sediments (Fig. 2D, Fig. 4, Fig. S6). XANES analysis indicates that most of the manganese is divalent Mn(II) and contained in manganoan calcite (Fig. S4). Iron oxides also host smaller amounts of manganese (visible in both EDS and electron microprobe maps; Fig. 4J).

Thus high bulk iron concentrations, previously inferred to represent carbonate dissolution and reprecipitation in low oxygen burial fluids, are better explained as artifacts of leaching procedures using strong acids which dissolve detrital hematite and minor authigenic hematite, associated with silts. In contrast, Mn enrichments reflect diagenetic addition of Mn^{+2} in the

earliest stages of sedimentation and cementation, presumably during or immediately after ooid deposition. In support of very early Mn cycling, we also observe Mn-rich banding within the dolomite ooids associated with the onset of the Shuram excursion at the top of the Khufai Formation (*44*)(Fig. 4E).

Phase-specific isotopic heterogeneity Some models suggest the Shuram excursion can be explained by the presence of isotopically light, secondary authigenic carbonate cements (*1, 7, 14*). We used Secondary Ion Mass Spectrometry (SIMS) to analyze disparate carbonate phases formed at different times (ooids, early Mn-rich pink cements, and clear blocky porosity-occluding cement). Authigenic explanations for the low δ^{13}C values characteristic of the Shuram excursion would predict the Mn-rich and/or porosity occluding blocky cements would have lower ^{13}C values relative to the ooids. This is not observed; in contrast, SIMS analysis of two samples from a similar stratigraphic horizon, but located $\sim$15 km apart, shows that ooids have similar carbon and oxygen isotopic compositions to both authigenic early manganese-rich pink cements, and porosity-occluding blocky spar cements (Fig. 4F,K, Fig. S6). The relatively homogeneous measurements of ooids and cements suggests that these phases reflect primary conditions and precipitated from similar fluids and temperatures or were pervasively altered by fluid-buffered diagenesis. Within the context of the above petrographic and trace element variability of these three phases, the former is more likely.

Crystallization temperature and fluid composition To further evaluate predictions of fluid- and sediment-buffered diagenesis at various points in the stratigraphy, carbonate clumped isotope thermometry analyses were performed on a range of carbonate facies. Carbonates with different initial characteristics (e.g., porosity, permeability, and mineralogy) will experience variable fluid-sediment interaction, which can result in co-variation of the fluid/sediment reaction temperature, carbonate $\delta^{18}O_{VPDB}$, and water $\delta^{18}O_{VSMOW}$. Cross-plots of these variables

will differentiate between packages of rocks that underwent fluid- or sediment-buffered alteration. If any of the intervals (including the transgressive dolomites (0 to $-5‰$) or the calcites of the nadir (~ -7 to $-12‰$) capturing parts of the Shuram excursion experienced fluid-buffered alteration in the Huqf as suggested in previous studies (*1, 3, 4, 15*), a diverse suite of samples should reveal a trend of increasing reaction temperature at relatively invariant $\delta^{18}O_{VSMOW}$ of water—near 0‰ if fluids are marine or more ^{18}O-depleted water if meteoric. If, instead, lithification or alteration occurred in sediment-buffered conditions, then water $\delta^{18}O$ and temperature will increase while carbonate $\delta^{18}O$ remains constant.

When plotted in this space, carbonates from the lower Khufai have the highest temperatures, are macroscopically coarsely crystalline, and are associated with petrographic observations indicating fluid flow including veining(Fig. 2F). Notably, $\delta^{13}C$ is not correlated with $\delta^{18}O$ in the lower Khufai Formation, despite a more fluid-buffered diagenetic regime and this interval is well below the onset of the Shuram excursion.

In contrast, the suite of pre-, onset-, and syn- Shuram-excursion carbonates analyzed from the upper Khufai, Shuram and lower Buah formations have data trends indicating sediment-buffered diagenesis (Fig. 2D). As a group, these carbonates show exceptional textural preservation, moderate clumped isotope temperatures (38–78°C) and precipitation from fluids with oxygen isotope compositions similar to the range observation across modern marine environments ($\delta^{18}O_{VSMOW}$ of water = 2 to +2‰)(Fig. 2D). It is important to note that the temperature measurements in Fig. 2 average the isotopic compositions of multiple carbonate phases—including primary ooids and other grains, mud and diagenetic cements (i.e. they are bulk measurements reflecting lithification). We note that mudstone, wackestone and finely laminated stromatolite samples with small crystal sizes and evidence for early lithification like tepee structures and carbonate intraclasts sit at the low-temperature end of the data trend in Fig. 2 (i.e. Fig. 2C,

Table S1) (*16*). Petrographic analysis of higher temperature samples indicate they are more heterogeneous, richer in secondary cements, and occur occasionally throughout the excursion (Fig. 2B,E,F) (*16*). The nadir carbonate in particular suggest sediment-buffered conditions (i.e. near constant δ^{18}O).

Diagenetic alteration of strata hosting the Shuram excursion While diagenesis has certainly played a role in the observed rock record in Oman, we argue based on the above observations that the Shuram excursion as expressed in Oman departs from the diagenetic expectations of post-depositional Shuram excursion models (Table 1). Models for a diagenetic origin for the Shuram excursion call on a range of post-depositional processes. Models that suggest the Shuram excursion is the result of fluid-buffered diagenesis by either meteoric (*2, 6*) or basinal fluids (*3*) predict fabric destruction, trace element homogeneity, and coarsening of crystal size (Table 1). Yet in the Huqf region of Oman, carbonates hosting the Shuram excursion are notable for their well-preserved fabrics, fine crystal sizes, and spatially-distinct trace element distributions (Figs. 2, 3, 4). Multiple fluid-buffered diagenetic models also predict low meteoric or high basinal fluid $\delta^{18}O_{VSMOW}$ values to explain the large negative δ^{18}O excursion (*2, 3*). These distinct oxygen isotope compositions are inconsistent with seawater-like fluid $\delta^{18}O_{VSMOW}$ values calculated from mineral δ^{18}O and Δ_{47}-temperature measurements of these strata (Fig. 4).

Models suggesting that the Shuram excursion is the result of syn-sedimentary remineralization of organic matter resulting in extremely light authigenic carbonates predict a significant difference in δ^{13}C between authigenic cements and primary carbonates (*1, 7, 14*)(Table 1). There is an early authigenic phase in shallow marine environments in Oman—pink Mn-rich cements—that partially cements ooids. However, our geochemical measurements document minimal isotopic heterogeneity across the multiple carbonate phases preserving the nadir (Fig. 3, Fig. S6). This isotopic homogeneity exists despite preserved elemental heterogeneity and

crystallographic differences between each phase, suggesting the isotopically light carbonates reflect precipitation from DIC rather than wholesale dissolution and reprecipitation (Fig. 3). Results are consistent with those from calcitic micrites in Australia (*46*). The only phase in those rocks with a distinct carbon isotopic composition are isotopically heavy dolomite rhombs of uncertain timing (*46*).

Another model has suggested that all carbonate sediments of this interval began as aragonite with light Ca isotopic compositions and high Sr concentrations, using the modern Bahamian platform as an analog, and some intervals underwent selective fluid-buffered alteration to produce heavy Ca isotopic intervals with low Sr concentrations (*4, 15, 47*)(Table 1). This model predicts that Oman, out of all the locations globally that preserve the Shuram excursion, hosts the most diagenetically altered strata because it has the highest Ca isotopic values (*15*). The interval with the heaviest Ca isotopic values, the dolomitic ooids capturing the onset of the excursion, would have experienced significant fluid flushing during a transformation from aragonite to dolomite. Instead, the above petrographic, geochemical, and isotopic observations suggest that three changes in the primary depositional mineralogy are a key component of the excursion (also see the Ocean Acidification and Recovery section below).

Evidence for a coupled climate-carbon cycle event Diagenetic alteration cannot account for our multi-proxy observations of the carbonates hosting the Shuram excursion in Oman. We instead explore our results in the context of the predictions of a coupled climate-carbon cycle model (Table 1) using the rich marine and terrestrial records of the PETM. We identify six predictions for a climate-carbon cycle perturbation, which have ramifications for the oceans, atmosphere, land, and biosphere. Alongside co-varying δ^{13}C and δ^{18}O isotopic records, these predictions are: [1] warming with an identifiable driver, [2] sea level rise and storms, [3] enhanced physical and chemical weathering, [4] ocean acidification, [5] anoxia, and [6] extinction

and radiation.

[1] Warming with Driver: To consider whether the Shuram excursion coincides with volcanic activity capable of driving a climate event, we built an inclusive database of Neoproterozoic occurrences of intrusive and extrusive igneous rocks. We classified each unit with compositional information and age constraints. The time interval of the Shuram excursion (574.0 ± 4.7 to 567.3 ± 3.0 Ma Ma) (*17*), coincides with a peak in occurrences of volcanic rocks, specifically, carbonatites (Fig. 5H). These CO_2-rich volcanic rocks are particularly abundant relative to other time intervals of the Neoproterozoic. Large, caldera-style carbonatite deposits can be found associated with the Central Iapetus Magmatic Province (*48*), including the Alnö complexes in Scandinavia (*49, 50*), the Vesely and Pogranichnoe complexes in Russia (*51*), the Sarfartoq complex in West Greenland (*52*), and those associated with the Pan-African orogeny in Africa (*53–56*) and Argentina (*57*). Carbonatite-derived zircons contribute to a significant peak at 576 Ma in detrital zircon spectra from Antarctica (*58*).

Our high resolution clumped-isotope thermometry (Δ_{47}) dataset from the Huqf area of Oman documents cooler temperatures in the pre-excursion and recovery strata compared with higher temperatures associated with the onset and nadir of the excursion (Fig. 2, Fig. S7). Interpreted within the context of a 600-million-year Δ_{47} record from Oman (*16*), solid state reordering is likely insignificant in the Huqf region (*42*). While we interpret the measured Δ_{47}-temperatures of these bulk rocks as somewhat elevated from depositional temperatures because they are composed of mixtures of primary sediments and shallow burial cements, the similarity of SIMS $\delta^{18}O$ data of ooids and cements suggests that the coldest clumped isotope temperatures in each time bin approach primary temperatures in this coastal, shallow marine, tropical environment. The broad change in temperature across the excursion may be significant because it is preserved in a range of lithofacies (both dolomites and calcites) with a range of primary porosities. Based on

these results we propose that the largest negative δ^{13}C excursion on record was coincident with an increase in shallow, coastal marine temperatures, perhaps as large as $\sim$12°Cfollowed by a cooling of $\sim$15°C(Fig. 4). Compiling the δ^{18}O of Ediacaran rock successions and accounting for mineralogy, many successions suggest warming followed by cooling of similar magnitudes assuming seawater δ^{18}O of -1.2‰(Fig. 5G, Fig. S8, Fig. S9). The carbonate δ^{18}O compositions in some sections are more clearly affected by deep burial alteration, however the broad pattern of concurrent δ^{13}C and δ^{18}O change is preserved (i.e. Death Valley region, Fig. S8, Fig. S9).

While we recognize that this temperature change is large, multiple aspects of the Ediacaran system may have contributed to its large magnitude relative to many Phanerozoic hyperthermals. Exact amounts of CO_2 from Ediacaran volcanic provinces are unknown, but carbonatites can have more CO_2 than mafic volcanics. There is also evidence for methane associated with Shuram excursion strata (*14*), which, if significant, could amplify rapid climate warming. Additionally, the DIC reservoir in the Ediacaran may have been larger (*59, 60*) than in the Cenozoic (*32*). Intriguingly, where the Shuram excursion is associated with carbonatites and warming, the Gaskiers glaciation and cooling, is associated with an increase mafic volcanic rocks (Fig. 5).

[2] Sea level rise and storms: Both sedimentological and geochemical evidence from Oman suggest sea level rise at the onset of the Shuram excursion. Facies associated with subaerial exposure, evaporation, and basinal restriction, including tepees, fenestral mudstones, intraclast conglomerates, and small, laterally linked, stromatolites, are capped by facies that record transgression during the onset of the excursion(Fig. 1, Fig. 5E) (*20*). Sedimentological features documenting sea level rise at the onset of the excursion are consistent features across many sections globally (*15, 19*). Sea level rise could be caused by thermal expansion of seawater from warming, melting of high latitude glaciers, or displacement from young, bouyant oceanic crust

associated with the opening of the Iapetus Ocean.

Facies present in the excursion nadir and recovery host storm deposits including hummocky cross-stratified silts, climbing wave ripples in deeper water environments and edgewise conglomerates across broad areas of Oman, Death Valley, NW Canada, and Australia (Fig. 1, Fig. 5E) (*15, 21, 22*). Strata containing these features are stacked for hundreds of vertical meters. A transition in the hydrologic cycle to more stormy conditions is consistent with warming, and is observed during the PETM (*30, 61*).

[3] Weathering: Grain-scale observations of the voluminous silts associated with the Shuram excursion nadir in Oman and Death Valley, including grain size and mineralogy, may be consistent with wind-blown loess filling accommodation in shallow water environments (*62, 63*)(Fig. 5E). A significant volume of detrital hematite is present in both locations (Fig. S5) (*63*), which we suggest is analogous to climate-driven detrital hematite enrichments within PETM deposits (*64*). Poorly weathered biotites, that are abundant within the siltstones associated with the nadir of the excursion (Fig. 4, Fig. S5) gradually disappear in the recovery, which we link to a switch from hot and dry conditions in the nadir of the excursion to warm and wet conditions in the recovery, again analagous to PETM deposits (*35–37, 65*). The Sr isotope record also indicates more radiogenic values consistent with chemical weathering (*66*)(Fig. 5D). The physical and geochemical observations of sediments deposited during the Shuram excursion are consistent with a concurrent land-based weathering and hydrologic cycle feedback that promoted global cooling through silicate weathering (*67*).

[4] Ocean Acidification and Recovery: We document textural, chemical, and isotopic evidence for primary mineralogical transformations associated with the Shuram excursion consistent with CO_2-driven ocean acidification and recovery. The onset of the excursion is captured

in a grainstone of radial, plumose dolomite ooids with small crystal sizes ($\delta^{13}C_{VPDB}$ = +2 to 6‰) (*44*) and micritic stromatolite bioherms (*20*). These are draped and overlain by poorly consolidated siltstones, representing a carbonate gap perhaps linked to acidification. After 10s of meters, the appearance of radial to banded radial calcitic ooids intercalated with siltstones with $\delta^{13}C_{VPDB}$ values of 10 to 12‰ may represent a shift from geochemical conditions disfavoring carbonate precipitation (*44*) to those favoring calcite precipitation (Fig. 3). Finally, the limestones capturing the recovery of the Shuram excursion consistently record high Sr concentrations and light Ca isotopic compositions, consistent with a precursor aragonite mineralogy, which requires a higher saturation state (*15, 19, 21*)(Fig. 5C). We interpret the mineralogical changes as evidence of a pH drop and recovery following chemical weathering, as in more recent ocean acidification events (*31, 36*). A smaller deep ocean carbonate reservoir (*60, 68*) may help explain why evidence for significant ocean acidification and a subsequent recovery can be found in such shallow environments. Consequences of acidification should be expected to vary in severity both regionally and with water depth.

[5] Anoxia: A temperature increase of 10-17°C in shallow coastal environments, as described above, would have implications for dissolved oxygen solubility. Early marine cements in the nadir have elevated manganese concentrations, indicating low oxygen conditions in the shallow sediments (Fig. 2, Fig. 4, Fig. S6). The early manganese-rich cement phase we have identified, suggests that anoxic conditions were prevalent in the shallow sediments and perhaps transiently in the water column. Yet the lack of pyrite implies sulfate reduction was less significant than manganese and iron reduction. Expanded anoxia associated with climate perturbations may amplify the importance of diagenetic processes (e.g. authigenic carbonate precipitation) and prevalence of isotopically light carbonates from enhanced organic remineralization (*24, 25*) or from methane clathrate destabilization (*14*)).

Most sediments of the Shuram excursion are extremely organic lean, unlike modern anoxic sediments. At higher temperatures, remineralization rates outpace carbon fixation rates and net primary productivity declines (*24, 25*). Both processes may explain the paucity of organic-rich black shales during the Shuram excursion, despite organic-rich intervals both prior to and after the Shuram excursion in deep-water Oman successions (*69*). The isotopic composition of preserved organic carbon is distinct in shallow and deep ocean records (*70*)(Fig. 5B). In Oman and China, inner and outer shelf inorganic δ^{13}C and $\delta^{13}C_{org}$ records are negatively correlated, whereas basinal records are positively correlated (*9, 71, 72*).

Spatial heterogeneity in elemental enrichments, organic abundance, and organic δ^{13}C differences between shallow and deep-water environments in Oman are consistent with a high temperature perturbation driving density and redox stratification in Ediacaran oceans. If carbonate deposition was initially sluggish and inhibited and the depositional area was largely limited to shallow water environments (*60, 68*), the residence time of carbon could have been longer, providing a mechanism to prolong the excursion.

[6] Extinction and Radiation: Coupled climate-carbon cycle perturbations have visible effects on the fossil record in the Phanerozoic, but extinctions are difficult to recognize in the non-skeletal, largely microscopic, fossil record of the Neoproterozoic. That said, evidence for extinction and subsequent origination is concurrent with the Shuram excursion. We estimate extinction and origination for microfossils, deep water Ediacaran fossils and shallow water Ediacaran fossils based on individual occurrence data (*42, 69, 73–77*)(Fig. 5A). Many ornamented, organic-walled acanthomorphic acritarch microfossils disappear from the paleontological record at the onset of the Shuram excursion (*77*). Within the nadir of the excursion, organic-walled acritarchs are simple and rare, while the recovery sees a diverse range of microfossils (*77, 78*). Macrofossils of algae, soft-bodied Ediacaran fauna, and the first biomineraliz-

ing organisms, *Cloudina* and *Namacalathus*, also appear following the recovery (*79*), although with new age constraints (*69*), many of the fauna appear in significantly younger strata (*80*). This pattern of origination following a hyperthermal is also observed following the PETM and other Phanerozoic warming events (*38, 81*). The appearance of large macroscopic Ediacaran fauna first in deep water environments in Newfoundland and NW Canada and then in shallow water environments globally (Fig. 5A), is parsimonious with an expectation that deep-water environments remained cooler during and following a temperature perturbation (*75, 82, 83*). The Shuram excursion may represent the best candidate documented thus far for a Precambrian mass extinction, followed by a recovery period with innovation, origination, and niche expansion. This suggests that the Shuram excursion represented a critical bottleneck and turning point for the evolutionary advances required for macroscopic, multicellular animal life.

Conclusions In summary, our climate driven model with coupled carbon cycle effects unifies a range of sedimentological, geochemical, and biological observations of the globally-distributed Shuram excursion. Our investigation finds little evidence to support hypotheses that interpret the Shuram excursion as a diagenetic event or artifact. Instead, sedimentological, geochemical, and paleontological records provide evidence of sea level rise, increased storm intensity, ocean acidification and anoxia, a concurrent terrestrial weathering event, and biotic extinction and origination. Abundant carbonatite eruptions concurrent with the excursion provide a potential driver. These observations pose challenges to our understanding of internal feedbacks in the carbon cycle and climate system in deep time. We contend that the Shuram excursion, the largest negative carbon isotope excursion in Earth History, is best understood as one of the most extreme hyperthermal events yet documented, and as such was likely both a critical bottleneck for complex life and also spurred origination of diverse soft-bodied Ediacaran fauna in its aftermath.

References and Notes

1. D. P. Schrag, J. A. Higgins, F. A. Macdonald, D. T. Johnston, Authigenic carbonate and the history of the global carbon cycle. *Science* **339**, 540–3 (2013).

2. L. P. Knauth, M. J. Kennedy, The late Precambrian greening of the Earth. *Nature* **460**, 728–732 (2009).

3. L. A. Derry, A burial diagenesis origin for the Ediacaran Shuram-Wonoka carbon isotope anomaly. *Earth Planet. Sci. Lett.* **294**, 152–162 (2010).

4. J. A. Higgins, C. L. Blättler, E. A. Lundstrom, D. P. Santiago-Ramos, A. A. Akhtar, A.-S. Crü Ger Ahm, O. Bialik, C. Holmden, H. Bradbury, S. T. Murray, P. K. Swart, Mineralogy, early marine diagenesis, and the chemistry of shallow-water carbonate sediments. *Geochim. Cosmochim. Acta* **220**, 512–534 (2018).

5. A.-S. C. Ahm, C. J. Bjerrum, C. L. Blättler, P. K. Swart, J. A. Higgins, Quantifying early marine diagenesis in shallow-water carbonate sediments. *Geochim. Cosmochim. Acta* **236**, 140–159 (2018).

6. G.-Y. Wei, J. Wang, N. J. Planavsky, M. Zhao, E. W. Bolton, L. Jiang, D. Asael, W. Wei, H.-F. Ling, On the origin of Shuram carbon isotope excursion in South China and its implication for Ediacaran atmospheric oxygen levels. *Precambrian Research* **375**, 106673 (2022).

7. L. Jiang, N. Planavsky, M. Zhao, W. Liu, X. Wang, Authigenic origin for a massive negative carbon isotope excursion. *Geology* **47**, 115–118 (2019).

8. D. H. Rothman, J. M. Hayes, R. E. Summons, Dynamics of the Neoproterozoic carbon cycle. *Proc. Natl. Acad. Sci. USA* **100**, 8124–8129 (2003).

9. D. A. Fike, J. P. Grotzinger, L. M. Pratt, R. E. Summons, Oxidation of the Ediacaran ocean. *Nature* **444**, 744–7 (2006).

10. C. J. Bjerrum, D. E. Canfield, Towards a quantitative understanding of the late Neoproterozoic carbon cycle. *Proc. Natl. Acad. Sci.* **108**, 5542–5547 (2011).

11. J. P. Grotzinger, D. A. Fike, W. W. Fischer, Enigmatic origin of the largest-known carbon isotope excursion in Earth's history (2011).

12. C. J. Bjerrum, D. E. Canfield, Towards a quantitative understanding of the late Neoproterozoic carbon cycle. *Proc. Natl. Acad. Sci.* **108**, 5542–5547 (2011).

13. T. F. Bristow, M. J. Kennedy, Carbon isotope excursions and the oxidant budget of the Ediacaran atmosphere and ocean. *Geology* **36**, 863–866 (2008).

14. H. Cui, A. J. Kaufman, S. Xiao, C. Zhou, X.-M. Liu, Was the Ediacaran Shuram Excursion a globally synchronized early diagenetic event? Insights from methane-derived authigenic carbonates in the uppermost Doushantuo Formation, South China (2016).

15. J. F. Busch, E. B. Hodgin, A.-S. C. Ahm, J. M. Husson, F. A. Macdonald, K. D. Bergmann, J. A. Higgins, J. V. Strauss, Global and local drivers of the Ediacaran Shuram carbon isotope excursion. *Earth and Planetary Science Letters* **579**, 117368 (2022).

16. K. D. Bergmann, S. A. Al Balushi, T. J. MacKey, J. P. Grotzinger, J. M. Eiler, A 600-million-year carbonate clumped-isotope record from the Sultanate of Oman. *J. Sediment. Res.* **88**, 960–979 (2018).

17. A. D. Rooney, M. D. Cantine, K. D. Bergmann, I. Gómez-Pérez, B. Al Baloushi, T. H. Boag, J. F. Busch, E. A. Sperling, J. V. Strauss, Calibrating the coevolution of Ediacaran life and environment. *Proc. Natl. Acad. Sci. U. S. A.* **117**, 16824–16830 (2020).

18. J. M. Husson, A. C. Maloof, B. Schoene, A syn-depositional age for Earth's deepest δ13C excursion required by isotope conglomerate tests. *Terra Nov.* **24**, 318–325 (2012).

19. K. Bergmann, R. Zentmyer, W. Fischer, The stratigraphic expression of a large negative carbon isotope excursion from the ediacaran johnnie formation, death valley. *Precambrian Res.* **188** (2011).

20. M. Osburn, J. Grotzinger, K. Bergmann, Facies, stratigraphy, and evolution of a middle ediacaran carbonate ramp: Khufai formation, sultanate of Oman. *Am. Assoc. Pet. Geol. Bull.* **98**, 1631–1667 (2014).

21. J. M. Husson, A. C. Maloof, B. Schoene, Stratigraphic expression of Earth's deepest δ^{13}C excursion in the Wonoka Formation of South Australia. *Am. J. Sci.* (2015).

22. E. Le Guerroué, P. A. Allen, A. Cozzi, Chemostratigraphic and sedimentological framework of the largest negative carbon isotopic excursion in earth history: The neoproterozoic Shuram formation (Nafun Group, Oman). *Precambrian Res.* **146**, 68–92 (2006).

23. E. Le Guerroué, P. A. Allen, A. Cozzi, Parasequence development in the Ediacaran Shuram Formation (Nafun Group, Oman): High-resolution stratigraphic test for primary origin of negative carbon isotopic ratios. *Basin Res.* **18**, 205–219 (2006).

24. S. M. Stanley, Relation of Phanerozoic stable isotope excursions to climate, bacterial metabolism, and major extinctions. *Proc. Natl. Acad. Sci. U. S. A.* **107**, 19185–19189 (2010).

25. S. Finnegan, D. A. Fike, D. Jones, W. W. Fischer, A Temperature-Dependent Positive Feedback on the Magnitude of Carbon Isotope Excursions. *Geosci. Canada* **39** (2012).

521 26. S. K. Turner, Pliocene switch in orbital-scale carbon cycle/climate dynamics. *Paleo-*
522 *ceanography* **29**, 1256–1266 (2014).

523 27. D. Evans, N. Sagoo, W. Renema, L. J. Cotton, W. Müller, J. A. Todd, P. K. Saraswati,
524 P. Stassen, M. Ziegler, P. N. Pearson, *et al.*, Eocene greenhouse climate revealed by cou-
525 pled clumped isotope-Mg/Ca thermometry. *Proceedings of the National Academy of Sci-*
526 *ences* **115**, 1174–1179 (2018).

527 28. G. N. Inglis, M. J. Carmichael, A. Farnsworth, D. J. Lunt, R. D. Pancost, A long-term,
528 high-latitude record of Eocene hydrological change in the Greenland region. *Palaeogeogr.*
529 *Palaeoclimatol. Palaeoecol.* **537** (2020).

530 29. A. Sluijs, U. Röhl, S. Schouten, H. J. Brumsack, F. Sangiorgi, J. S. Sinninghe Damsté,
531 H. Brinkhuis, late Paleocene - Early Eocene paleoenvironments with special emphasis on
532 the Paleocene-Eocene thermal maximum (Lomonosov Ridge, Integrated Ocean Drilling
533 Program Expedition 302). *Paleoceanography* **23**, PA1S11 (2008).

534 30. M. J. Carmichael, R. D. Pancost, D. J. Lunt, Changes in the occurrence of extreme precip-
535 itation events at the Paleocene–Eocene thermal maximum. *Earth and Planetary Science*
536 *Letters* **501**, 24–36 (2018).

537 31. J. C. Zachos, U. Röhl, S. A. Schellenberg, A. Sluijs, D. A. Hodell, D. C. Kelly, E. Thomas,
538 M. Nicolo, I. Raffi, L. J. Lourens, H. McCarren, D. Kroon, Paleoclimate: Rapid acidifica-
539 tion of the ocean during the paleocene-eocene thermal maximum. *Science* **308**, 1611–1615
540 (2005).

541 32. D. A. Harper, B. Cascales-Miñana, T. Servais, Early Palaeozoic diversifications and ex-
542 tinctions in the marine biosphere: A continuum of change. *Geol. Mag.* **157**, 5–21 (2020).

543 33. X. Zhou, E. Thomas, R. E. Rickaby, A. M. Winguth, Z. Lu, I/Ca evidence for upper ocean
544 deoxygenation during the PETM. *Paleoceanography* **29**, 964–975 (2014).

545 34. A. Sluijs, L. Van Roij, G. Harrington, S. Schouten, J. Sessa, L. LeVay, G.-J. Reichart,
546 C. Slomp, Warming, euxinia and sea level rise during the Paleocene–Eocene Thermal
547 Maximum on the Gulf Coastal Plain: implications for ocean oxygenation and nutrient
548 cycling. *Climate of the Past* **10**, 1421–1439 (2014).

549 35. V. Pujalte, J. Baceta, B. Schmitz, A massive input of coarse-grained siliciclastics in the
550 Pyrenean Basin during the PETM: the missing ingredient in a coeval abrupt change in
551 hydrological regime. *Climate of the Past* **11**, 1653–1672 (2015).

552 36. D. C. Kelly, J. C. Zachos, T. J. Bralower, S. A. Schellenberg, Enhanced terrestrial weath-
553 ering/runoff and surface ocean carbonate production during the recovery stages of the
554 Paleocene-Eocene thermal maximum. *Paleoceanography* **20** (2005).

555 37. R. Wieczorek, M. S. Fantle, L. R. Kump, G. Ravizza, Geochemical evidence for volcanic
556 activity prior to and enhanced terrestrial weathering during the Paleocene Eocene Thermal
557 Maximum. *Geochimica et Cosmochimica Acta* **119**, 391–410 (2013).

558 38. R. Speijer, C. Scheibner, P. Stassen, A.-M. M. Morsi, Response of marine ecosystems to
559 deep-time global warming: A synthesis of biotic patterns across the Paleocene-Eocene
560 thermal maximum (PETM). *Austrian Journal of Earth Sciences* **105**, 6–16 (2012).

561 39. M. R. Osburn, J. Owens, K. D. Bergmann, T. W. Lyons, Dynamic changes in sulfate sulfur
562 isotopes preceding the Ediacaran Shuram Excursion. *Geochim. Cosmochim. Acta* (2015).

563 40. S. J. Burns, A. Matter, Carbon isotopic record of the latest Proterozoic from Oman. *Eclo-*
564 *gae Geol. Helv.* **86**, 595–607 (1993).

41. E. Le Guerroué, P. A. Allen, A. Cozzi, Chemostratigraphic and sedimentological framework of the largest negative carbon isotopic excursion in earth history: The neoproterozoic Shuram formation (Nafun Group, Oman). *Precambrian Res.* **146**, 68–92 (2006).

42. Materials and methods are available as supplementary materials at the science advances website .

43. A. Cozzi, P. A. Allen, J. P. Grotzinger, Understanding carbonate ramp dynamics using δ^{13}C profiles: Examples from the Neoproterozoic Buah Formation of Oman. *Terra Nov.* **16**, 62–67 (2004).

44. J. Wilcots, P. Gilbert, K. Bergmann, Nanoscale crystal fabric preserved in dolomite ooids at the onset of the Ediacaran Shuram excursion. *Geophysical Research Letters* (PrePrint).

45. Y. Fang, H. Xu, Dissolved silica-catalyzed disordered dolomite precipitation. *American Mineralogist: Journal of Earth and Planetary Materials* **107**, 443–452 (2022).

46. J. M. Husson, B. J. Linzmeier, K. Kitajima, A. Ishida, A. C. Maloof, B. Schoene, S. E. Peters, J. W. Valley, Large isotopic variability at the micron-scale in 'Shuram' excursion carbonates from South Australia. *Earth Planet. Sci. Lett.* **538** (2020).

47. A.-S. C. Ahm, C. J. Bjerrum, C. L. Blättler, P. K. Swart, J. A. Higgins, Quantifying early marine diagenesis in shallow-water carbonate sediments. *Geochim. Cosmochim. Acta* **236**, 140–159 (2018).

48. N. Youbi, R. E. Ernst, U. Söderlund, M. A. Boumehdi, A. A. Lahna, C. C. G. Tassinari, W. El Moume, M. K. Bensalah, The Central Iapetus magmatic province: An updated review and link with the ca. 580 Ma Gaskiers glaciation. *Mass Extinctions, Volcanism, and Impacts: New Developments* **544**, 35–66 (2020).

587 49. A. M. Andersson, A. Malehmir, V. R. Troll, M. Dehghannejad, M. Andersson,
588 A. Malehmir, V. R. Troll, M. Dehghannejad, C. Juhlin, M. Ask, Carbonatite ring-
589 complexes explained by caldera-style volcanism. *Sci. Rep.* **3**, 1–9 (2013).

590 50. M. Andersson, *3D Structure and Emplacement of the Alnö Alkaline and Carbonatite*
591 (2015).

592 51. A. G. Doroshkevich, G. S. Ripp, N. V. Vladykin, V. M. Savatenkov, Sources of the Late
593 Riphean carbonatite magmatism of Northern Transbaikalia: Geochemical and isotope-
594 geochemical data. *Geochemistry Int.* **49**, 1195–1207 (2011).

595 52. K. Secher, L. M. Heaman, T. F. D. Nielsen, S. M. Jensen, F. Schjøth, R. A. Creaser, Tim-
596 ing of kimberlite, carbonatite, and ultramafic lamprophyre emplacement in the alkaline
597 province located 64°-67° N in southern West Greenland. *Lithos* **112**, 400–406 (2009).

598 53. K. Attoh, F. Corfu, P. M. Nude, U-Pb zircon age of deformed carbonatite and alkaline
599 rocks in the Pan-African Dahomeyide suture zone, West Africa. *Precambrian Res.* **155**,
600 251–260 (2007).

601 54. K. Burke, L. D. Ashwal, S. J. Webb, New way to map old sutures using deformed alkaline
602 rocks and carbonatites. *Geology* **31**, 391–394 (2003).

603 55. A. B. Kampunzu, M. N. Makutu, G. Rocci, J. Kramers, F. Pineau, I. Louaradf, F. Tembo,
604 Neoproterozoic Alkaline and Carbonatite Magmatism Along the Western Rift in Central-
605 Eastern Africa: Break-up of Rodinia Supercontinent and Reconstruction of Gondwana.
606 *Gondwana Res.* **1**, 155–156 (1997).

607 56. J. J. Veevers, Pan-Gondwanaland post-collisional extension marked by 650-500 Ma alka-
608 line rocks and carbonatites and related detrital zircons: A review. *Earth-Science Rev.* **83**,
609 1–47 (2007).

610 57. C. Casquet, R. J. Pankhurst, C. Galindo, C. Rapela, C. M. Fanning, E. Baldo, J. Dahlquist,
611 J. M. G. Casado, F. Colombo, A deformed alkaline igneous rock-carbonatite complex
612 from the Western Sierras Pampeanas, Argentina: Evidence for late Neoproterozoic open-
613 ing of the Clymene Ocean? *Precambrian Res.* **165**, 205–220 (2008).

614 58. T. Paulsen, C. Deering, J. Sliwinski, O. Bachmann, M. Guillong, Evidence for a spike in
615 mantle carbon outgassing during the Ediacaran period. *Nature Geoscience* **10**, 930–934
616 (2017).

617 59. T. T. Isson, N. J. Planavsky, L. Coogan, E. Stewart, J. Ague, E. Bolton, S. Zhang,
618 N. McKenzie, L. Kump, Evolution of the global carbon cycle and climate regulation on
619 earth. *Global Biogeochemical Cycles* **34**, e2018GB006061 (2020).

620 60. K. D. Bergmann, J. Wilcots, T. Pico, N. Boekelheide, N. T. Anderson, M. D. Cantine, S. L.
621 Goldberg, B. Keller, A. B. Jost, A. Eyster, Onset of carbonate biomineralization drove
622 global reorganization of sedimentation and subsidence patterns. *Preprint at 10.1002/es-*
623 *soar.10511913.1* (2022).

624 61. B. Schmitz, V. Pujalte, Abrupt increase in seasonal extreme precipitation at the Paleocene-
625 Eocene boundary. *Geology* **35**, 215–218 (2007).

626 62. M. D. Cantine, J. B. Setera, J. A. VanTongeren, C. Mwinde, K. D. Bergmann, Grain
627 size and transport biases in an Ediacaran detrital zircon record. *Journal of Sedimentary*
628 *Research* **91**, 913–928 (2021).

629 63. K. Bergmann, J. Grotzinger, W. Fischer, Biological influences on seafloor carbonate pre-
630 cipitation. *Palaios* **28** (2013).

631 64. E. Dallanave, L. Tauxe, G. Muttoni, D. Rio, Silicate weathering machine at work: rock
632 magnetic data from the late Paleocene–early Eocene Cicogna section, Italy. *Geochemistry,*
633 *Geophysics, Geosystems* **11** (2010).

634 65. C. Robert, J. P. Kennett, Antarctic subtropical humid episode at the Paleocene-Eocene
635 boundary: clay-mineral evidence. *Geology* **22**, 211–214 (1994).

636 66. X. Chen, Y. Zhou, G. A. Shields, Progress towards an improved Precambrian seawater
637 87Sr/86Sr curve. *Earth-Science Reviews* **224**, 103869 (2022).

638 67. J. C. Walker, P. B. Hays, J. F. Kasting, A negative feedback mechanism for the long-term
639 stabilization of Earth's surface temperature. *J. Geophys. Res.* **86**, 9776–9782 (1981).

640 68. A. J. Ridgwell, Carbonate Deposition, Climate Stability, and Neoproterozoic Ice Ages.
641 *Science* **302**, 859–862 (2003).

642 69. A. D. Rooney, M. D. Cantine, K. D. Bergmann, I. Gómez-Pérez, B. A. Baloushi, T. H.
643 Boag, J. F. Busch, E. A. Sperling, J. V. Strauss, Calibrating the coevolution of Ediacaran
644 life and environment. *Proc. Natl. Acad. Sci. U. S. A.* **117**, 16824–16830 (2020).

645 70. G. Jiang, X. Wang, X. Shi, S. Xiao, S. Zhang, J. Dong, The origin of decoupled carbonate
646 and organic carbon isotope signatures in the early Cambrian (ca. 542-520Ma) Yangtze
647 platform. *Earth Planet. Sci. Lett.* **317-318**, 96–110 (2012).

648 71. C. Lee, G. D. Love, W. W. Fischer, J. P. Grotzinger, G. P. Halverson, Marine organic
649 matter cycling during the Ediacaran Shuram excursion. *Geology* **43**, 1103–1106 (2015).

650 72. C. Lee, D. A. Fike, G. D. Love, A. L. Sessions, J. P. Grotzinger, R. E. Summons, W. W.
651 Fischer, Carbon isotopes and lipid biomarkers from organic-rich facies of the Shuram
652 Formation, Sultanate of Oman. *Geobiology* **11**, 406–419 (2013).

73. L. A. Riedman, P. M. Sadler, Global species richness record and biostratigraphic potential of early to middle Neoproterozoic eukaryote fossils. *Precambrian Res.* **319**, 6–18 (2018).

74. C. Yang, A. D. Rooney, D. J. Condon, X.-H. Li, D. V. Grazhdankin, F. T. Bowyer, C. Hu, F. A. Macdonald, M. Zhu, The tempo of Ediacaran evolution. *Science Advances* **7**, eabi9643 (2021).

75. F. Zhang, H. Wang, Y. Ye, Y. Liu, Y. Lyu, Y. Deng, D. Lyu, X. Wang, H. Wu, S. Deng, *et al.*, Did high temperature rather than low O_2 hinder the evolution of eukaryotes in the Precambrian? *Precambrian Research* **378**, 106755 (2022).

76. S. Xiao, B. Shen, Q. Tang, A. J. Kaufman, X. Yuan, J. Li, M. Qian, Biostratigraphic and chemostratigraphic constraints on the age of early Neoproterozoic carbonate successions in North China. *Precambrian Res.* **246**, 208–225 (2014).

77. K. A. McFadden, J. Huang, X. Chu, G. Jiang, A. J. Kaufman, C. Zhou, X. Yuan, S. Xiao, Pulsed oxidation and biological evolution in the Ediacaran Doushantuo Formation. *Proc. Natl. Acad. Sci.* **105**, 3197–3202 (2008).

78. N. J. Butterfield, J. P. Grotzinger, Palynology of the Huqf Supergroup, Oman. *Geol. Soc. London, Spec. Publ.* **366**, 251–263 (2012).

79. S. Xiao, G. M. Narbonne, C. Zhou, M. Laflamme, D. V. Grazhdankin, M. Moczydlowska-Vidal, H. Cui, Towards an Ediacaran time scale: Problems, protocols, and prospects. *Episodes* **39**, 540–555 (2016).

80. Z. An, G. Jiang, J. Tong, L. Tian, Q. Ye, H. Song, H. Song, Stratigraphic position of the Ediacaran Miaohe biota and its constrains on the age of the upper Doushantuo δ^{13}C anomaly in the Yangtze Gorges area, South China. *Precambrian Res.* **271**, 243–253 (2015).

81. H. Song, D. B. Kemp, L. Tian, D. Chu, H. Song, X. Dai, Thresholds of temperature change for mass extinctions. *Nature communications* **12**, 1–8 (2021).

82. T. H. Boag, R. G. Stockey, L. E. Elder, P. M. Hull, E. A. Sperling, Oxygen, temperature and the deep-marine stenothermal cradle of Ediacaran evolution. *Proc. R. Soc. B Biol. Sci.* **285**, 20181724 (2018).

83. C. Simpson, Adaptation to a viscous Snowball Earth ocean as a path to complex multicellularity. *The American Naturalist* **198**, 590–609 (2021).

84. S. T. Kim, J. R. O'Neil, Equilibrium and nonequilibrium oxygen isotope effects in synthetic carbonates. *Geochim. Cosmochim. Acta* **61**, 3461–3475 (1997).

85. J. Horita, Oxygen and carbon isotope fractionation in the system dolomite–water–CO_2 to elevated temperatures. *Geochim. Cosmochim. Acta* **129**, 111–124 (2014).

86. T. Ishikawa, Y. Ueno, T. Komiya, Y. Sawaki, J. Han, D. Shu, Y. Li, S. Maruyama, N. Yoshida, Carbon isotope chemostratigraphy of a Precambrian/Cambrian boundary section in the Three Gorge area, South China: Prominent global-scale isotope excursions just before the Cambrian Explosion. *Gondwana Res.* **14**, 193–208 (2008).

87. R. Kikumoto, M. Tahata, M. Nishizawa, Y. Sawaki, S. Maruyama, D. Shu, J. Han, T. Komiya, K. Takai, Y. Ueno, Nitrogen isotope chemostratigraphy of the Ediacaran and Early Cambrian platform sequence at Three Gorges, South China. *Gondwana Res.* **25**, 1057–1069 (2014).

88. J. P. Pu, S. A. Bowring, J. Ramezani, P. Myrow, T. D. Raub, E. Landing, A. Mills, E. Hodgin, F. A. Macdonald, Dodging snowballs: Geochronology of the Gaskiers glaciation and the first appearance of the Ediacaran biota. *Geology* **44**, 955–958 (2016).

698 89. Y. Sawaki, T. Ohno, M. Tahata, T. Komiya, T. Hirata, S. Maruyama, B. F. Windley, J. Han,
699 D. Shu, Y. Li, The Ediacaran radiogenic Sr isotope excursion in the Doushantuo Formation
700 in the Three Gorges area, South China. *Precambrian Res.* **176**, 46–64 (2010).

701 90. D. A. Fike, J. P. Grotzinger, L. M. Pratt, R. E. Summons, Oxidation of the Ediacaran
702 ocean. *Nature* **444**, 744–747 (2006).

703 91. C. Li, D. S. Hardisty, G. Luo, J. Huang, T. J. Algeo, M. Cheng, W. Shi, Z. An, J. Tong,
704 S. Xie, N. Jiao, T. W. Lyons, Uncovering the spatial heterogeneity of Ediacaran carbon
705 cycling. *Geobiology* **15**, 211–224 (2017).

706 92. B. G. Pokrovskii, V. A. Melezhik, M. I. Bujakaite, Carbon, oxygen, strontium, and sulfur
707 isotopic compositions in late Precambrian rocks of the Patom Complex, central Siberia:
708 Communication 1. results, isotope stratigraphy, and dating problems. *Lithol. Miner. Re-*
709 *sour.* **41**, 450–474 (2006).

710 93. M. Tahata, Y. Ueno, T. Ishikawa, Y. Sawaki, K. Murakami, J. Han, D. Shu, Y. Li, J. Guo,
711 N. Yoshida, T. Komiya, Carbon and oxygen isotope chemostratigraphies of the Yangtze
712 platform, South China: Decoding temperature and environmental changes through the
713 Ediacaran. *Gondwana Res.* **23**, 333–353 (2013).

714 94. X. Wang, G. Jiang, X. Shi, S. Xiao, Paired carbonate and organic carbon isotope variations
715 of the Ediacaran Doushantuo Formation from an upper slope section at Siduping, South
716 China. *Precambrian Res.* **273**, 53–66 (2016).

717 95. G. M. Cox, G. P. Halverson, A. Poirier, D. Le Heron, J. V. Strauss, R. Stevenson, A model
718 for Cryogenian iron formation. *Earth Planet. Sci. Lett.* **433**, 280–292 (2016).

719 96. P. C. Boggiani, C. Gaucher, A. N. Sial, M. Babinski, C. M. Simon, C. Riccomini, V. P.
720 Ferreira, T. R. Fairchild, Chemostratigraphy of the Tamengo Formation (Corumbá Group,

Brazil): A contribution to the calibration of the Ediacaran carbon-isotope curve. *Precambrian Res.* **182**, 382–401 (2010).

97. J. J. Veevers, Pan-Gondwanaland post-collisional extension marked by 650-500 Ma alkaline rocks and carbonatites and related detrital zircons: A review. *Earth-Science Rev.* **83**, 1–47 (2007).

98. R. E. Ernst, K. L. Buchan, Large mafic magmatic events through time and links to mantle-plume heads. *Spec. Pap. Geol. Soc. Am.* **352**, 483–575 (2001).

99. R. E. Ernst, K. Bell, Large igneous provinces (LIPs) and carbonatites. *Mineral. Petrol.* **98**, 55–76 (2010).

100. A. R. Woolley, B. a. Kjarsgaard, Carbonatite Occurrences of the World :. *Nat. Hist.* (2008).

101. D. Li, H. F. Ling, G. A. Shields-Zhou, X. Chen, L. Cremonese, L. Och, M. Thirlwall, C. J. Manning, Carbon and strontium isotope evolution of seawater across the Ediacaran-Cambrian transition: Evidence from the Xiaotan section, NE Yunnan, South China. *Precambrian Res.* **225**, 128–147 (2013).

102. J. P. Hodych, R. A. Cox, Ediacaran U–Pb zircon dates for the Lac Matapédia and Mt. St.-Anselme basalts of the Quebec Appalachians: support for a long-lived mantle plume during the rifting phase of Iapetus opening. *Can J Earth Sci* **581**, 565–581 (2007).

103. K. Secher, L. M. Heaman, T. F. D. Nielsen, S. M. Jensen, F. Schjøth, R. A. Creaser, Timing of kimberlite, carbonatite, and ultramafic lamprophyre emplacement in the alkaline province located 64°-67° N in southern West Greenland. *Lithos* **112**, 400–406 (2009).

104. E. McClellan, E. Gazel, The Cryogenian intra-continental rifting of Rodinia: Evidence from the Laurentian margin in eastern North America. *Lithos* **206-207**, 321–337 (2014).

105. S. Tappe, A. Steenfelt, T. Nielsen, Asthenospheric source of Neoproterozoic and Mesozoic kimberlites from the North Atlantic craton, West Greenland: New high-precision U-Pb and Sr-Nd isotope data on perovskite. *Chem. Geol.* **320-321**, 113–127 (2012).

106. J. G. Meert, T. H. Torsvik, The making and unmaking of a supercontinent: Rodinia revisited. *Tectonophysics* **375**, 261–288 (2003).

107. C. R. Calver, L. P. Black, J. L. Everard, D. B. Seymour, U-Pb zircon age constraints on late Neoproterozoic glaciation in Tasmania. *Geology* **32**, 893–896 (2004).

108. C. R. Calver, J. L. Crowley, M. T. Wingate, D. A. Evans, T. D. Raub, M. D. Schmitz, Globally synchronous marinoan deglaciation indicated by U-Pb geochronology of the cottons Breccia, Tasmania, Australia. *Geology* **41**, 1127–1130 (2013).

109. S. Meffre, N. G. Direen, A. J. Crawford, V. Kamenetsky, Mafic volcanic rocks on King Island, Tasmania: Evidence for 579 Ma break-up in east Gondwana. *Precambrian Res.* **135**, 177–191 (2004).

110. K. Attoh, F. Corfu, P. M. Nude, U-Pb zircon age of deformed carbonatite and alkaline rocks in the Pan-African Dahomeyide suture zone, West Africa. *Precambrian Res.* **155**, 251–260 (2007).

111. E. Eneroth, O. M. Svenningsen, Equatorial Baltica in the Vendian: Palaeomagnetic data from the Sarek Dyke Swarm, northern Swedish Caledonides. *Precambrian Res.* **129**, 23–45 (2004).

112. D. P. Gladkochub, S. A. Pisarevsky, T. V. Donskaya, R. E. Ernst, M. T. D. Wingate, U. Soderlund, A. M. Mazukabzov, E. V. Sklyarov, M. A. Hamilton, J. A. Hanes, Proterozoic mafic magmatism in Siberian craton: An overview and implications for paleocontinental reconstruction. *Precambrian Res.* **183**, 660–668 (2010).

113. V. Yarmolyuk, V. Kovalenko, E. Sal nikova, A. Nikiforov, A. Kotov, N. Vladykin, *DOKLADY EARTH SCIENCES C/C OF DOKLADY-AKADEMIIA NAUK* (INTERPERIODICA PUBLISHING, 2006), vol. 404, p. 1031.

114. D. V. Metelkin, V. A. Vernikovsky, A. Y. Kazansky, Neoproterozoic evolution of Rodinia: constraints from new paleomagnetic data on the western margin of the Siberian craton. *Russ. Geol. Geophys.* **48**, 32–45 (2007).

115. N. V. Vladykin, A. B. Kotov, A. S. Borisenko, V. V. Yarmolyuk, N. P. Pokhilenko, E. B. Sal'nikova, A. V. Travin, S. Z. Yakovleva, Age boundaries of formation of the Tomtor alkaline-ultramafic pluton: U-Pb and 40Ar/39Ar geochronological studies. *Dokl. Earth Sci.* **454**, 7–11 (2014).

116. V. V. Vrublevskii, V. V. Reverdatto, a. E. Izokh, I. F. Gertner, D. S. Yudin, P. a. Tishin, Neoproterozoic carbonatite magmatism of the Yenisei Ridge, Central Siberia: 40Ar/39Ar geochronology of the Penchenga rock complex. *Dokl. Earth Sci.* **437**, 443–448 (2011).

117. J. P. Donatti-Filho, S. Tappe, E. P. Oliveira, L. M. Heaman, Age and origin of the Neoproterozoic Brauna kimberlites: Melt generation within the metasomatized base of the São Francisco craton, Brazil. *Chemical Geology* **353**, 19–35 (2013).

118. A. D. Nozhkin, O. M. Turkina, T. B. Bayanova, N. G. Berezhnaya, A. N. Larionov, A. A. Postnikov, A. V. Travin, R. E. Ernst, Neoproterozoic rift and within-plate magmatism in the Yenisei Ridge: implications for the breakup of Rodinia. *Russ. Geol. Geophys.* **49**, 503–519 (2008).

119. a. E. Vernikovskaya, V. M. Datsenko, V. a. Vernikovsky, N. Y. Matushkin, Y. M. Laevsky, I. V. Romanova, a. V. Travin, K. V. Voronin, E. N. Lepekhina, Magmatism evolution and carbonatite-granite association in the neoproterozoic active continental margin of the

789 Siberian craton: Thermochronological reconstructions. *Dokl. Earth Sci.* **448**, 161–167
790 (2013).

791 120. F. V. Kaminsky, S. M. Sablukov, L. I. Sablukova, D. M. D. Channer, Neoproterozoic
792 'anomalous' kimberlites of Guaniamo, Venezuela: Mica kimberlites of 'isotopic transi-
793 tional' type. *Lithos* **76**, 565–590 (2004).

794 121. S. W. Denyszyn, H. C. Halls, D. W. Davis, D. A. Evans, Paleomagnetism and U-Pb
795 geochronology of Franklin dykes in high arctic Canada and Greenland: A revised age
796 and paleomagnetic pole constraining block rotations in the Nares Strait region. *Can. J.*
797 *Earth Sci.* **46**, 689–705 (2009).

798 122. A. A. Ariskin, Y. A. Kostitsyn, E. G. Konnikov, L. V. Danyushevsky, S. Meffre, G. S.
799 Nikolaev, A. McNeill, E. V. Kislov, D. A. Orsoev, Geochronology of the Dovyren intrusive
800 complex, northwestern Baikal area, Russia, in the Neoproterozoic. *Geochemistry Int.* **51**,
801 859–875 (2013).

802 123. Z.-X. Li, S. Bogdanova, A. Collins, A. Davidson, B. De Waele, R. Ernst, I. Fitzsimons,
803 R. Fuck, D. Gladkochub, J. Jacobs, *et al.*, Assembly, configuration, and break-up history
804 of Rodinia: a synthesis. *Precambrian research* **160**, 179–210 (2008).

805 124. C. Li, P. Peng, G. Sheng, J. Fu, Y. Yan, A molecular and isotopic geochemical study
806 of Meso- to Neoproterozoic (1.73-0.85 Ga) sediments from the Jixian section, Yanshan
807 Basin, North China. *Precambrian Res.* **125**, 337–356 (2003).

808 125. J. K. Park, K. L. Buchan, S. S. Harlan, A proposed giant radiating dyke swarm fragmented
809 by the separation of Laurentia and Australia based on paleomagnetism of ca. 780 Ma mafic
810 intrusions in western North America. *Earth Planet. Sci. Lett.* **132**, 129–139 (1995).

126. Y. Zhang, D. A. Rodionov, M. S. Gelfand, V. N. Gladyshev, Comparative genomic analyses of nickel, cobalt and vitamin B12 utilization. *BMC Genomics* **10**, 78 (2009).

127. C. L. Zhang, X. H. Li, Z. X. Li, S. N. Lu, H. M. Ye, H. M. Li, Neoproterozoic ultramafic-mafic-carbonatite complex and granitoids in Quruqtagh of northeastern Tarim Block, western China: Geochronology, geochemistry and tectonic implications. *Precambrian Res.* **152**, 149–169 (2007).

128. A. Fabris, S. Constable, C. Conor, A. Woodhouse, S. Hore, M. Fanning, Age, origin, emplacement and mineral potential of the Oodla Wirra Volcanics, Nackara Arc, central Flinders Ranges. *MESA J.* **37**, 44–52 (2005).

129. T. H. Boag, S. A. Darroch, M. Laflamme, Ediacaran distributions in space and time: Testing assemblage concepts of earliest macroscopic body fossils. *Paleobiology* **42**, 574–594 (2016).

130. M. Foote, Origination and extinction components of taxonomic diversity: general problems. *Paleobiology* **26**, 74–102 (2000).

131. J. P. Grotzinger, Upward shallowing platform cycles: a response to 2.2 billion years of low-amplitude, high-frequency (Milankovitch band) sea level oscillations. *Paleoceanography* **1**, 403–416 (1986).

132. A. Cozzi, J. P. Grotzinger, P. A. Allen, Evolution of a terminal Neoproterozoic carbonate ramp system (Buah Formation, Sultanate of Oman): Effects of basement paleotopography. *Bull. Geol. Soc. Am.* **116**, 1367–1384 (2004).

133. A. C. Ries, R. M. Shackleton, Structures in the Huqf-Haushi Uplift, east Central Oman. *Geol. Soc. London, Spec. Publ.* **49**, 653–663 (1990).

833 134. V. P. Wright, A. C. Ries, S. G. Munn, Intraplatformal basin-fill deposits from the Infra-
834 cambrian Huqf Group, east central Oman. *Geol. Soc. London, Spec. Publ.* **49**, 601–616
835 (1990).

836 135. G. E. Gorin, L. G. Racz, M. R. Walter, Late Precambrian-Cambrian sediments of Huqf
837 Group, Sultanate of Oman. *Am. Assoc. Pet. Geol. Bull.* **66**, 2609–2627 (1982).

838 136. J. Dubreuilh, J. P. Platel, J. Le Métour, J. Roger, R. Wyns, F. Béchennec, A. Berthiaux,
839 Explanatory notes to the Geological map of Khaluf, Sheet NF 40-15, scale 1: 250000,
840 *Tech. rep.*, Directorate General of minerals, Oman ministry of petroleum and minerals
841 (1992).

842 137. G. D. Love, E. Grosjean, C. Stalvies, D. a. Fike, J. P. Grotzinger, A. S. Bradley, A. E. Kelly,
843 M. Bhatia, W. Meredith, C. E. Snape, S. a. Bowring, D. J. Condon, R. E. Summons, Fossil
844 steroids record the appearance of Demospongiae during the Cryogenian period. *Nature*
845 **457**, 718–21 (2009).

846 138. E. Grosjean, G. D. Love, C. Stalvies, D. A. Fike, R. E. Summons, Origin of petroleum in
847 the Neoproterozoic–Cambrian South Oman Salt Basin. *Org. Geochem.* (2009).

848 139. J. D. Hemingway, G. A. Henkes, A disordered kinetic model for clumped isotope bond
849 reordering in carbonates. *Earth and Planetary Science Letters* **566**, 116962 (2021).

850 140. D. A. Stolper, J. M. Eiler, The kinetics of solid-state isotope-exchange reactions for
851 clumped isotopes: A study of inorganic calcites and apatites from natural and experi-
852 mental samples. *Am. J. Sci.* **315**, 363–411 (2015).

853 141. G. A. Henkes, B. H. Passey, E. L. Grossman, B. J. Shenton, A. Perez-Huerta, T. E. Yancey,
854 Temperature limits for preservation of primary calcite clumped isotope paleotemperatures.
855 *Geochim. Cosmochim. Acta* **139**, 362–382 (2014).

142. M. K. Lloyd, J. M. Eiler, P. I. Nabelek, Clumped isotope thermometry of calcite and dolomite in a contact metamorphic environment. *Geochim. Cosmochim. Acta* **197**, 323–344 (2017).

143. M. Bonifacie, D. Calmels, J. Eiler, Clumped Isotope Thermometry of Marbles as an Indicator of the Closure Temperatures of Calcite and Dolomite with Respect to Solid-State Reordering of C–O Bonds. *Mineral. Mag.* **77**, 735 (2013).

144. W. Visser, Burial and thermal history of Proterozoic source rocks in Oman. *Precambrian Res.* **54**, 15–36 (1991).

145. M. G. McCarron, The sedimentology and chemostratigraphy of the Nafun Group, Huqf Supergroup, Oman, Phd thesis, Oxford University (1999).

146. K. D. T. Nguyen, S. A. Morley, C. H. Lai, M. S. Clark, K. S. Tan, A. E. Bates, L. S. Peck, Upper temperature limits of tropical marine ectotherms: Global warming implications. *PLoS One* **6** (2011).

Acknowledgements: K.D.B. thanks John Grotzinger for initial support with the geology of Oman and John Eiler for support with the clumped isotope measurements published in (*16*). Both provided feedback on early versions of this manuscript. C. Ma, J. Hurowitz, N. Kitchen, and Y. Guan provided assistance with analytical measurements. JC Creveling, Dave Johnston, and Andy Knoll provided feedback on early versions of this manuscript. Portions of this research were carried out at the Stanford Synchrotron Radiation Lightsource, a Directorate of SLAC National Accelerator Laboratory and an Office of Science User Facility operated for the US Department of Energy Office of Science by Stanford University. S. Webb and J. Johnson helped with the XANES measurements at SLAC and provided standard data. We thank Petroleum Development Oman employees for helpful discussions, particularly Irene Gomez Perez, Joachim Amthor, Gideon Lopes Cardozo, Erwin Adams, Gordon Forbes, Badar Al Balushi, and Sven Scholten. Funding for analytical measurements was provided by the Agouron Institute and NASA Astrobiology Institute. We thank the Ministry of Energy and Minerals of the Sultanate of Oman and Petroleum Development Oman for permission to publish this manuscript and for fieldwork and analytical support. Thure Cerling, Lou Derry, and an anonymous reviewer provided helpful criticism of an earlier verison of this manuscript. **Funding:** K.D.B. acknowledges funding from the Packard Foundation and NASA Exobiology Grant 80NSSC19K0464. M.D.C. was supported by a National Defense Science and Engineering Graduate Fellowship; K.D.B. and M.R.O. were supported by National Science Foundation Graduate Research Fellowships during their PhDs; **Author Contributions:** K.D.B. and W.F. conceptualized the study. K.D.B., M.R.O., and M.D.C. conducted field investigations. K.D.B, N.B., and J.W. contributed formal analysis, software, and visualization. K.D.B. wrote the original draft. All authors reviewed and edited the manuscript; **Data and materials availability:** All data are provided in the main text or in the supplementary materials. Data, figures, and code are available at Open Science Framework (link) for reviewers and will be made publicly

894 available on manuscript acceptance.

895 **Supplementary Materials** :

896 Materials and Methods

897 Figs. S1 - S9

898 References (83 - 146)

Test	Climate	Diagenetic Models			
	this study	*Deep Burial (Derry et al., 2010)*	*Authigenic (Schrag et al., 2013)*	*Meteoric (Knauth & Kennedy, 2008)*	*Selective (Higgins et al., 2018)*
Sedimentology & Stratigraphy	reflect environmental & climatic change	coarsely crystalline	authigenic phases like nodules and concretions	coarsely crystalline	coarsely crystalline in low Sr intervals
Petrography	well preserved phases precipitated from seawater	dissolution-large crystals	authigenic carbonate	dissolution-reprecipitation, leaching	dissolution-reprecipitation within low Sr intervals
Mineralogy	controlled by pH and alkalinity of seawater	no prediction	no prediction	aragonite to calcite	sediment-buffered interval keeps high Sr
Trace elements	distinct across petrographic phases	homogenized	distinct in authigenic phase	homogenized	homogenized within low Sr interval
Isotopic variability	homogenous from DIC reservoir	homogenized	^{13}C distinct in authigenic phase	homogenized	homogenized within low Sr interval
Temperature and fluid $\delta^{18}O$ composition	warming during excursion, marine $\delta^{18}O$	high burial T, heavy fluid $\delta^{18}O$	moderate T, marine $\delta^{18}O$	low T, meteoric $\delta^{18}O$	T and fluid $\delta^{18}O$ vary
Burial environment	sediment-buffered	sediment-buffered	sediment-buffered	fluid-buffered	fluid- and sediment-buffered intervals

1

899

900 **Table 1. Proposed models of the Shuram excursion** Tests of previous (diagenetic) and pro-
901 posed (climate) mechanisms for the Shuram excursion using a variety of observations.

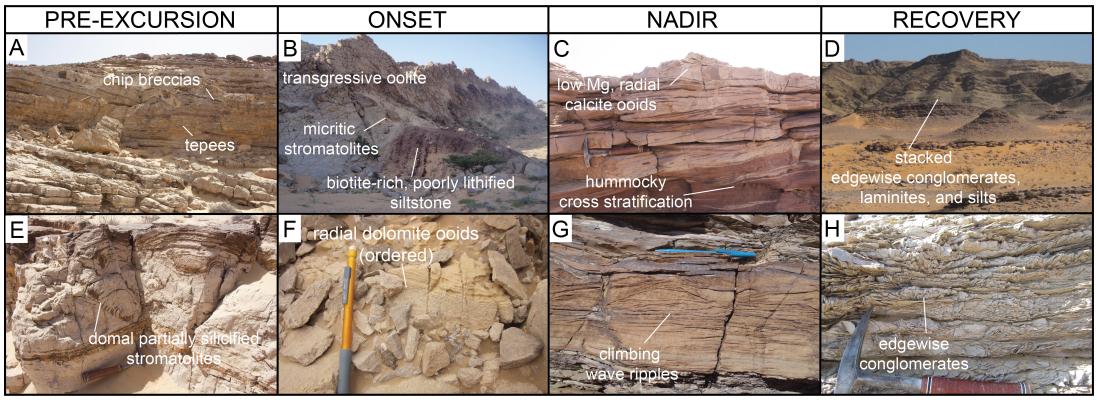

Fig. 1. The stratigraphic expression of the Shuram excursion in the Huqf region of Oman (**A, E**) Pre-excursion peritidal dolomite facies including stromatolites, tepees, chip breccias. (**B, F**) transgressive dolomitic oolite capped by micritic stromatolites and red silts. (**C**) Cross-stratified calcitic oolite capping red siltstones of the Shuram Formation. (**D, H**) Stacked storm-derived edgewise conglomerates, silts, and crinkly laminites at Mukhaibah Dome. (**G**) Outer shelf Shuram Formation carbonate beds with climbing wave ripples in green siltstones of the Oman Mountains.

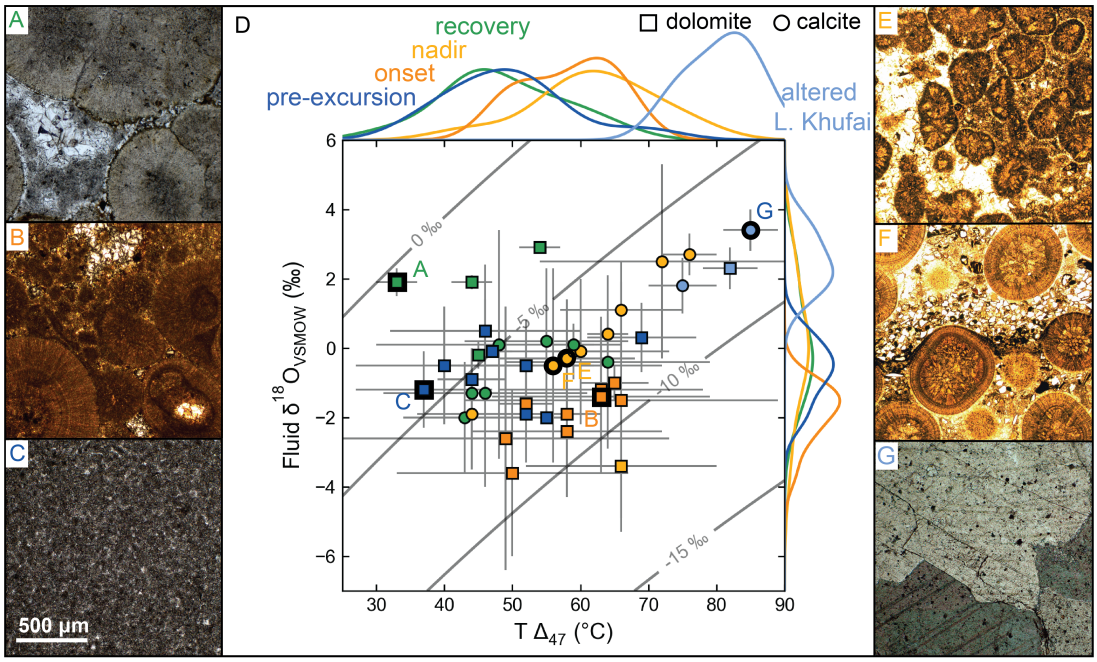

Fig. 2. Petrographic character and burial alteration environment of inner shelf carbonates hosting the excursion (**A**) Thin-section photomicrograph of dolomitic conophyton stromatolite from the recovery of the excursion. (**B**) Dolomitic oolite hosting the onset of the excursion with silica cement under cross polarized light. (**C**) Mudstone from the pre-excursion peritidal Upper Khufai Fm. (**D**) Clumped isotope temperature vs. calculated water $\delta^{18}O_{VSMOW}$ with isopleths of carbonate $\delta^{18}O_{VPDB}$. The populations all tend to along $\delta^{18}O_{VPDB}$ isopleths indicating sediment-buffered alteration. Both the onset and nadir populations are warmer than the populations of pre-excursion and recovery. (**E**) Calcitic oolite from the nadir of the excursion with two distinct cement phases (early Mn-rich cement and later blocky cement). (**F**) Calcitic oolite from the nadir of the excursion intercalated with silt. (**G**) Coarsely recrystallized calcite from the lower Khufai Formation. The scale bar applies to all images.

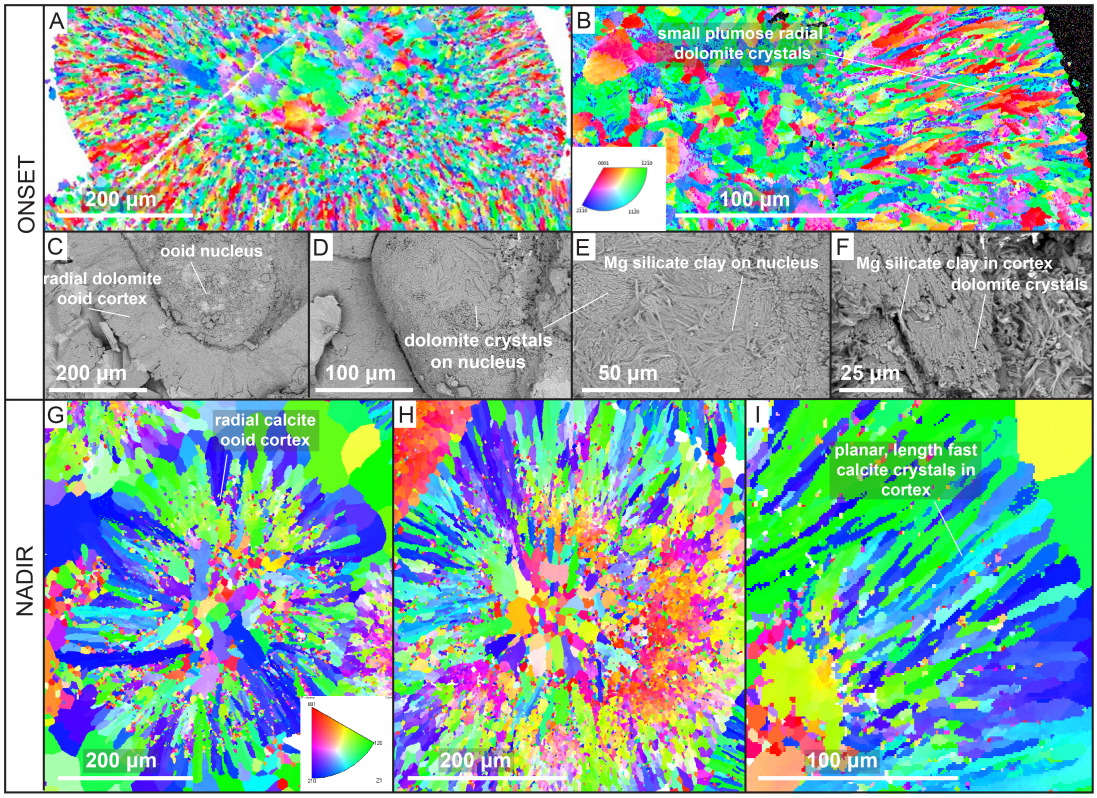

922

923 **Fig. 3. Mineralogy and crystal orientation of dolomite and calcite ooids recording the**
924 **excursion.** (**A, B**) Electron backscatter diffraction (EBSD) crystal orientation maps of dolomite
925 ooids from the onset of the excursion with radial crystal orientations in the cortex, see also (*44*).
926 (**C, D, E, F**) SEM images of cryo-fractured dolomite ooids with a Mg silicate clay in both the
927 nucleus and cortex. (**G, H, I**) EBSD crystal orientation maps of calcite ooids from the nadir.

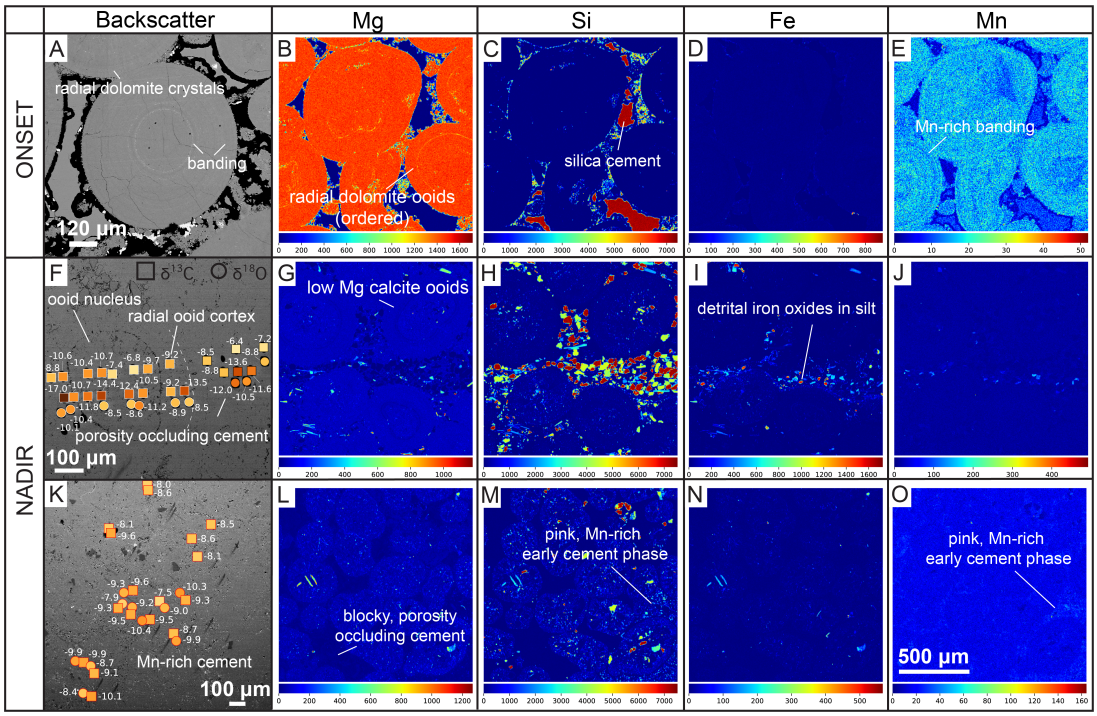

928

929 **Fig. 4. In situ isotopic and trace metal variations.** (**A**) SEM backscatter images of dolomite
930 ooids from the onset of the excursion. (**B, C, D, E**) Elemental maps of Mg, Si, Fe and Mn.
931 Visible silica cement as in Fig. 2B. (**F, K**) SEM backscatter images of calcite ooids from the
932 nadir of the excursion with SIMS spot analyses of carbon (squares) and oxygen (circles) isotopic
933 composition of ooids (white outline), blocky cement (black outline), and early Mn-rich cement
934 (red outline). (**G, H, I, J, L, M, N, O**) Respective elemental maps of each nadir oolite. Visible
935 detrital minerals around the ooids include quartz, biotite, and iron and titanium oxides. Scale
936 bar on the elemental map applies to all maps.

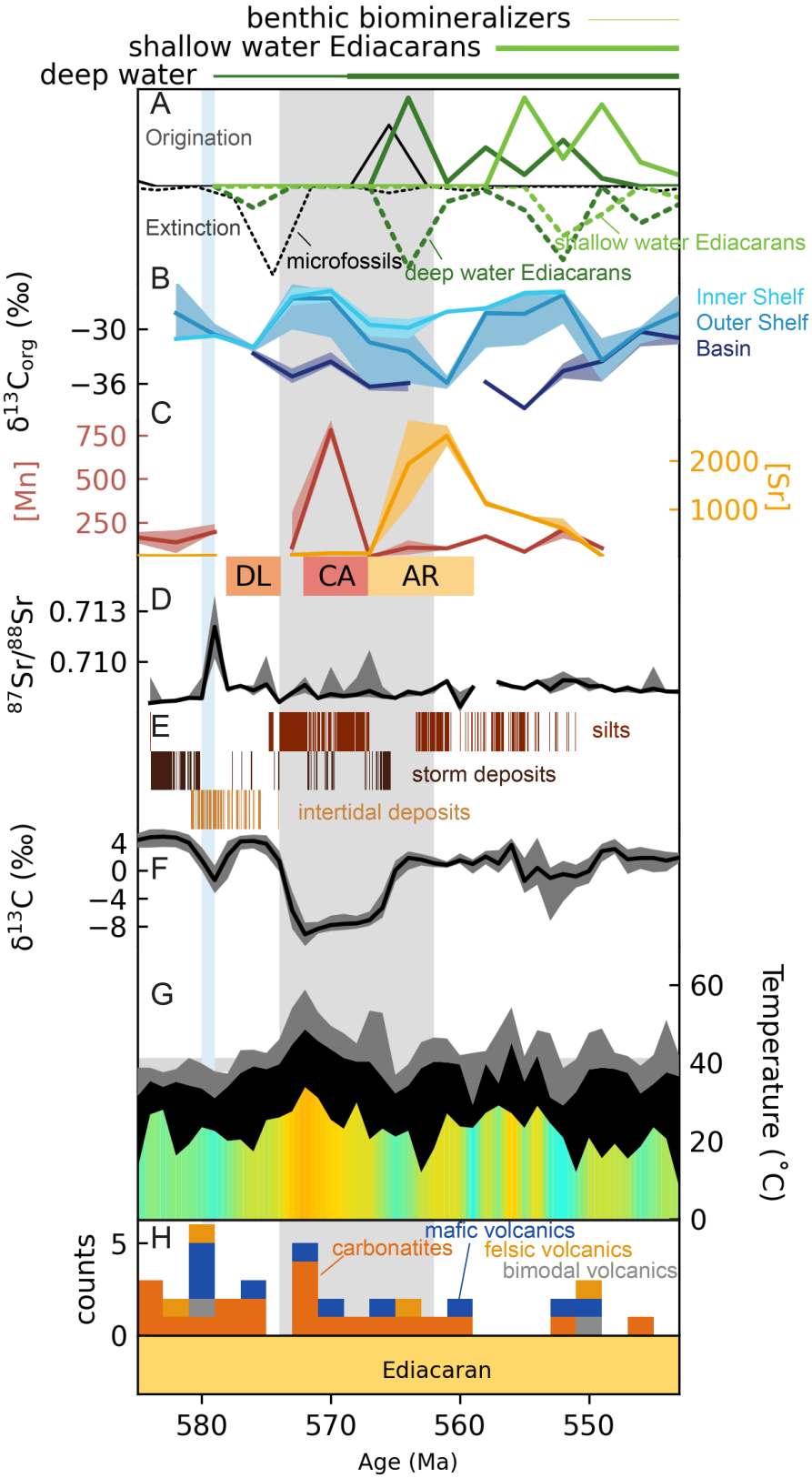
benthic biomineralizers
shallow water Ediacarans
deep water
A
Origination
Extinction
microfossils
deep water Ediacarans
shallow water Ediacarans
B
Inner Shelf
Outer Shelf
Basin
δ13Corg (‰)
−30
−36
C
[Mn]
750
500
250
2000
1000
[Sr]
DL
CA
AR
D
87Sr/88Sr
0.713
0.710
E
silts
storm deposits
intertidal deposits
δ13C (‰)
4
0
−4
−8
F
G
60
40
20
0
Temperature (°C)
H
counts
5
0
mafic volcanics
carbonatites
felsic volcanics
bimodal volcanics
Ediacaran
580
570
560
550
Age (Ma)

Fig. 5. Evidence for a coupled climate-carbon cycle perturbation. (**A**) Extinction and origination based on fossil occurrence data in 3 Myr bins (*42*). (**B**) $\delta^{13}C_{org}$ from three depositional environments in Oman and China. (**C**) Composite Mn and Sr (ppm) records and suggested primary mineralogies dominating shallow marine environments through time (DL: dolomite, CA: calcite, AR: aragonite). (**D**) $^{87}Sr/^{86}Sr$ from (*66*). (**E**) Sedimentologic evidence for silt, storm deposits, and intertidal deposits in Central Oman. (**F**) $\delta^{13}C$ composite record. (**G**) Composite temperature (°C record excluding Ediacaran sites from Laurentia and Russia. The 1^{st} to 25th quantiles (black) and 25th to 50th quantiles (grey) of shallow marine temperatures estimated from $\delta^{18}O$ using quantile regression on points within 1 Myr windows sampled each 1 Myr. (**H**) Counts of extrusive volcanic provinces. Blue line marks the Gaskiers glaciation. Grey band is the approximate duration of the Shuram excursion. The shaded regions in B, C, D, and F are the 25th to 75th quantiles and median using quantile regression on points within 1 Myr windows sampled each 1 Myr (D, F) or within 3 Myr windows sampled each 3 Myr (B, C). (*42*).

Supplementary Materials for: The Shuram excursion: A response to climate extremes at the dawn of animal life

Authors:

Kristin D. Bergmann, Magdalena Osburn, Julia Wilcots,

Marjorie Cantine, Nicholas Boekelheide Woodward W. Fischer,

Magali Bonifacie

1 Materials and Methods

Stratigraphic measurement, sample collection and preparation Carbonate samples were collected from outcrop locations from the Huqf Outcrop area in the winters of 2010 and 2011. Stratigraphic sections were measured and sampled in stratigraphic height at Mukhaibah Dome (MD) and Khufai Dome (KD) in the Huqf Outcrop area. Hand samples were cut to expose an unweathered face prior to further sampling or analysis. A variety of lithofacies were analyzed from each stratigraphic section including mudstone, stromatolite boundstone, oolitic grainstone, siltstone, sandstone and edgewise conglomerate and features like tepees. The textural range sampled was in part driven by necessity because no single facies persists through the entire excursion at high resolution. The added benefit of analyzing a range of carbonate facies is an improved understanding of preservation biases associated with specific carbonate textures and different primary porosities that lead to varying contributions from secondary cements. All carbonate samples analyzed in this study were composed of $> 70\%$ primary carbonate grains or micrite and $< 30\%$ post depositional diagenetic cements (estimated visually in hand sample and thin section) except when secondary veins were specifically targeted for analysis. To create the records of environment-specific deposits, a composite stratigraphic column of the MD and KD sections was created (Fig. 5F). Intertidal deposits included tepees and oncolites, which in the Khufai Formation are associated with the shallowest tufted and irregular laminites and tepees.

Storm deposits included edgewise conglomerates, intraclast conglomerates, ooid grainstones, and hummocky cross stratification. Silt deposits included silt and cover, which we assume to primarily be silt in the Shuram and Buah formations in the Huqf.

Bulk powder x-ray diffraction (XRD) XRD measurements were made on each powder used for clumped isotope measurements on a PANalytical X'Pert Pro within the Material Science at the California Institute of Technology. Scans were run from 5–70° 2θ with a step size of 0.008 and a scan step time of 10.16 s. A Cu anode was used at 45 kV and 40 mA. A zero-background silicon plate was used for all measurements because of our small sample sizes. Mineralogical phases were initially identified using the X'Pert Highscore IDMin function in Jade. To determine relative abundances of calcite and dolomite in each sample, the relative peak height intensities of the major calcite and dolomite peaks at 29.5° 2θ and 30.7° 2θ, respectively, were used(23). Mixtures of known compositions of 100%, 80%, 60%, 40%, 20% and 0% calcite with dolomite were used to create the following relationship of peak height to % dolomite for the PANalytical X'Pert Pro setup at Caltech:

$$\%Dolomite = \frac{\frac{R.I.CaMg(CO_3)_2}{R.I.CaMg(CO_3)_2+CaCO_3} - 0.0526}{0.0099}$$

90% of the samples analyzed were pure end-members of either calcite or dolomite. For the 10% of samples that were a mixture of both calcite and dolomite, the acid digestion fractionation for δ^{18}O and min-water fractionation factor for all mixtures in the clumped isotope calculations were made assuming 100% composition of the dominant mineralogy. This will introduce a systematic bias for values reported from those samples, but very few samples have subequal ($<$70:30) carbonate mineral abundances.

SEM/electron microprobe A ZEISS 1550 VP Field Emission Scanning Electron Microscope (SEM) equipped with an Oxford INCA Energy 300 x-ray Energy Dispersive Spectrometer

(EDS) system within the California Institute of Technology Geological and Planetary Sciences Division Analytical Facility was used for high-resolution imaging of each sample. Images were collected at a working distance between 7-9 mm using a Quadrant Back Scattering Detector (QBSD). In addition EDS spectroscopy measurements of individual minerals were made to identify the types of detrital minerals present in a given sample. Electron Backscatter Diffraction (EBSD) analyses were performed using Oxford AZtecHKL acquisition software on samples with 2.5-5 μm carbon coats. Kikuchi bands were collected using 20kV accelerating voltage at 70° tilt with step sizes between 0.4 and 1 μm. Data were analyzed using Oxford HKL Channel 5 software to map grain boundaries and preferred orientation.

Cryo-fracturing experiments were conducted on dolomitic oolites from Khufai Dome and Wadi Shuram. Samples were submerged in liquid nitrogen and then broken on removal. The broken face was gold coated and imaged on a Phenom XL SEM at MIT.

Quantitative elemental spot analysis and elemental mapping on the various carbonate components to assess trace metal variability between textures was conducted on the JEOL JXA-8200 Electron Microprobe. For all quantitative results, the accelerating voltage was 15 kV, the beam current was 20 nA, and the beam size was 1 μm. The CITZAF method was used for matrix correction. Sample standards for the five chemical elements analyzed, included: calcite for Ca, dolomite for Mg, siderite for Fe, rhodochrosite for Mn, strontianite for Sr, and anhydrite for S. Ca had an average detection limit of 177 ppm, Mg–283 ppm, Fe–323 ppm, Mn–300 ppm, Sr–589 ppm, and S–104 ppm.

Bulk powder inductively coupled plasma optical emission spectroscopy (ICP-OES) Bulk ICP measurements were completed at Actlabs and at the Jet Propulsion Laboratory (JPL) on splits of the same drilled powder. The Actlabs method digested up to 0.5 g of sample with aqua regia (HCl + NO3) for 2 hours at 95°C. Partial reactions are possible for some silicates with

this dissolution method. Samples were then analyzed using a Varian ICP-OES for 35 elements. To target only the bulk limestone between 10 and 80 mg of material was digested in 10% acetic acid for 24 hours at 25°C at the California Institute of Technology. Samples were then filtered to remove particulate oxides and diluted with HCl to minimize introduction issues with the Ar plasma source. Samples were analyzed at the Jet Propulsion Laboratory using a Thermo iCAP 6300 radial view ICP-OES with a Cetac ASX 260 autosampler with solutions aspirated to the Ar plasma using a peristaltic pump. Three standard solutions of 0.5 ppm. 5 ppm and 50 ppm of Mn, Al, Ca, K, Mg, S, Fe and Na, and three standard solutions of 0.1 ppm, 1 ppm and 10 ppm Sr in an acetic-HCl solution to matrix match were run between every 8 sample unknowns.

Bulk powder x-ray absorption near edge spectroscopy X-ray absorption near-edge spectroscopy (XANES) was conducted at the Stanford Synchrotron Radiation Lightsource (SSRL) on beam line 4-1 on five representative bulk powdered samples from the Shuram Formation in Central Oman. Samples were collected using a 3 mm rotary drill bit and further powdered using a mortar and pestle. The powdered samples were spread in a monolayer over Scotch tape and then covered with a second layer of Scotch tape. Approximately 8–16 Scotch tape layers were used for each sample, to maximize both absorbance and transmission. We used a silicon 220 Φ= 90 crystal and x-ray absorption spectra (XAS) were collected on a Ge multi-element detector for fluorescence and on an absorption detector for transmission spectra. A collimating mirror was used to reduce beam harmonics. XANES spectra of both Fe and Mn spectra were generated for each sample with a scan from 6310–7502 eV. Samples were then normalized for each element and compared to XANES spectra of known standards analyzed under similar conditions.

Secondary ion mass spectrometry (SIMS) In situ analysis of $\delta^{13}C_{VPDB}$ and $\delta^{18}O_{VPDB}$ was conducted using SIMS analysis on a Cameca 7f-GEO in the Center for Microanalysis at the California Institute of Technology. The Cameca 7f-GEO was run at a mass resolving power for

C of 3000 and for O of 1800. Two thick sections of samples from the nadir of the excursion from the Mukhaibah Dome (MD) and Khufai Dome (KD) sections were embedded with in-house carbonate standards prior to polishing (Fig. S9). A 10 kV Cs^+ beam was held at 0.4 nA for C analyses and 1.1 nA for O analyses for spot sizes of 30 µm and 40 µm, respectively. Each spot was pre-sputtered for 120 s. Oxygen was measured on a two Faraday cups for a count time of 0.96 s for ^{16}O and 4.96 s for ^{18}O using a fast mass peak switching system. Carbon was measured on a single EM with a count time of 0.96 s for ^{12}C and 10.0 s for ^{13}C. Secondary ions were collected at 9 kV. 10 measurements of sample unknowns were bracketed with 4 standard analyses. Standard deviation was better than 1‰ for $\delta^{13}C$ and $\delta^{18}O$ for each of the 8 standard analyses bracketing sets of unknowns.

Carbonate clumped isotope thermometry All samples plotted were previously published in (*16*). Refer to that reference for methods, data processing, analysis and petrographic and hand sample context.

Carbonate carbon and oxygen isotopic analysis In addition to the clumped isotope measurements described above, new high resolution $\delta^{13}C$ and $\delta^{18}O$ data across the Shuram and Buah formations was analyzed at the California Institute of Technology on a ThermoFinnigan Delta V Plus attached to a ThermoFinnigan GasBench II. This data was combined with isotopic data from the Khufai Formation (*39*). For the samples analyzed at Caltech, approximately 300 µg of carbonate were weighed into gas vials, flushed with UHP He for 5 minutes and reacted with 100% H_3PO_4 at 78°Cfor 1 hour within the ThermoFinnigan GasBench II. Three standards were run at the beginning of an 88 sample run and then 8 unknown samples were bracketed by 1 standard. Standard reproducibility was better than 0.2‰ in $\delta^{13}C$ and better than 0.35‰ and 0.5‰ for $\delta^{18}O$ for two in-house standards. Additional samples were analyzed at the University of California, Riverside and University of Nevada, Las Vegas using a similar ThermoFinnigan

GasBench setup. Samples analyzed at the University of Michigan weighing a minimum of 10 µg were placed in stainless steel boats. Samples were roasted at 200°Cin vacuo for one hour to remove volatile contaminants and water. Samples were then placed in individual borosilicate reaction vessels and reacted at 77° ± 1°Cwith 4 drops of anhydrous phosphoric acid for 8 minutes for calcite (12 minutes for dolomites) in a ThermoFinnigan MAT Kiel IV preparation device coupled directly to the inlet of a ThermoFinnigan MAT 253 triple collector IRMS. ^{17}O corrected data are corrected for acid fractionation and source mixing by calibration to a best-fit regression line defined by two NBS standards, NBS18 and NBS19. Data are reported in delta notation relative to VPDB. Precision and accuracy of data are monitored through daily analysis of a variety of powdered carbonate standards. At least four standards are reacted and analyzed daily. Measured precision is maintained at better than 0.1‰ for both carbon and oxygen isotope compositions.

Isotopic and Elemental Compilation A literature search was conducted to locate published carbonate isotopic and trace element data (i.e. Mn, Sr, etc.) and $\delta^{13}C_{org}$ from platform carbonates for Fig. 5. The δ^{18}O data from these individual studies of bulk rock δ^{13}C had not been previously compiled in a systematic way with a high-resolution age model. Study level isotopic datasets from the literature were digitized into .csv files, and metadata were added (location, mineralogy, type of material, Formation name, etc.). We calculated temperature using a water $\delta^{18}O_{VSMOW}$ value of -1.2‰. We used mineral-specific fractionation factors for calcite samples (*84*) and dolomite samples (*85*). $\delta^{13}C_{org}$ data are divided into inner shelf environments (*9*), outer shelf environments (*70, 86, 87*), and basinal environments (*71*). Ages of Gaskiers are from (*88*).

Data included in isotopic and elemental compilation :

Ediacaran: (*39, 70, 71, 74, 86, 87, 89–96*)

$^{87}Sr/^{86}Sr$: (*66*)

Age Model We created a consistent age model for all individual studies and opted not to use previously published age models individual authors may have created. Age models were built using information provided within the datasets, stratigraphic columns, and text of compiled articles. For all points in the dataset, ages were interpolated using a linear model assuming a constant sedimentation rate between tie points. Sedimentation rates were error checked for consistency. The age model for compiled δ^{18}O Proterozoic datasets utilized U/Pb and Re/Os ages from the published literature (*69, 74*) and δ^{13}C excursions were used to build a new age model for each study, except (*66, 74*).

Volcanism Compilation A literature search was conducted to locate published dates of Neoproterozoic igneous activity including both extrusive and intrusive deposits. Information includes name, location, size estimates if they exist, type of deposit, age and error on the age.

Data included in volcanism compilation :

(*51, 97–128*)

Per Capita Extinction and Origination Rates We first calculated FAD and LAD from occurrences we tabulated for Neoproterozoic microfossils from (*73, 76, 77*) and Neoproterozoic Ediacaran fauna from (*129*), separated into deep water and shallow water occurrences. We calculate per capita extinction and origination rates (*130*) on these three compilations using 3 Myr bins without subsampling. The age constraints we used for fossil occurrences in the Neoproterozoic are included in a Supplemental Table and in the OSF repository. Results are normalized to the largest per capita extinction or origination rate in each of the four records.

2 Supplementary information

Geologic Setting In central Oman, the Khufai Formation is composed of shallow-water carbonates deposited on a carbonate ramp. The carbonates in the Huqf show a generalized upward shallowing of the lithofacies and lateral progradation. The lower Khufai Formation is composed of medium to thick intraclast wackestone event beds deposited below storm weather wave base (*20*). In contrast, the middle and upper Khufai Formation was deposited in a peritidal environment with minimal accommodation space, and restriction and evaporation. These rocks display petrographic evidence for an early, fabric-retentive, dolomite formation process (*20,44*). Lithofacies include cross-bedded oncolite grainstone, tufted laminite, domal stromatolites, intraclast conglomerate and structures including teepees associated with evaporite mineral pseudomorphs and brecciation (Fig. 1, Fig. S1) (*20*). The most proximal facies in the Upper Khufai Formation (i.e., teepees and breccia) are overlain by aggradding stromatolites and oolitic grainstone marking a sequence boundary exists where the depositional environment changes from one dominated by exposure to one characterized by slow flooding and increased accommodation space (*20*). The carbonate strata above the sequence boundary preserve the initial decline in δ^{13}C and δ^{18}O values of the Shuram excursion. The dolomitic lithofacies of the uppermost Khufai, including stromatolites and cross-stratified ooid grainstone record $\delta^{13}C_{VPDB}$ values as low as -8.5‰ (Fig. 1, Fig. S1). One would predict this transition from a restricted evaporative environment to a flooded platform in closer connection with open marine water would be accompanied by an isotopic change in the fluid oxygen isotope composition. The maximal transgression and flooding is coincident with the introduction of massive, poorly bedded red siltstone deposits and a general loss of carbonate lithofacies marking the start of the siliciclastic dominated Shuram Formation (Fig. 1) (*20, 41*). The middle and upper Shuram Formation is better exposed in outcrop and consists of repeated parasequences of hummocky cross-stratified

siltstone capped by trough to planar cross-stratified limestone ooid grainstone with $\delta^{13}C_{VPDB}$ values as low as -12‰ (Fig. 1, Fig. S1) (*23, 41*). The siltstone contains abundant evidence for soft sediment deformation including ball and pillow structures (*23*). The recovery of the Shuram excursion occurs in the lower Buah Formation, which is also composed of shallow-water carbonates that indicate a general upward shallowing of the lithofacies. The lowermost Buah is composed of limestone crinkly laminite and edgewise conglomerate, a lithofacies interpreted as a partially lithified seafloor that is reworked and stacked on edge by oscillatory wave action (Fig. 1, Fig. S1) (*131*). This reworking of the seafloor likely occurred during storm events. The gradual isotopic recovery continues above a sequence boundary that shows a rapid increase in accommodation space, a shutoff in the siliciclastic input and the aggradation of large reefal stromatolite mounds filled in with trough cross-stratified grainstone shoals (Fig. S1).

In the Oman Mountains the Khufai Formation is thinner, completely limestone and is predominantly intraclast wackestone and mudstone deposited as turbidites below storm weather wave base. The Upper Khufai Formation is marked by successive large-scale (3 m) slump beds and in a few locations including Wadi Bani Awf significant coarse grained sandstone beds (*20, 41*). The Shuram Formation is dominantly composed of siltstones alternating with ripple-stratified silty carbonate grainstone beds with gutter casts on bed bottoms. The ripples indicate significant aggradation during ripple formation producing asymmetrical climbing wave ripple morphologies (Fig. 1, Fig. S1) (*41*). The Buah Formation has a broadly similar lithofacies progression to the Huqf outcrop area with more significant lithofacies differences between Wadi Hajir and Wadi Bani Awf, the latter being more distal (*43, 132*).

Considerations for interpreting the Δ_{47} results Here we discuss potential effects of burial history, diffusive solid state reordering, and mixing on the interpretation of the clumped isotope signal across the Shuram excursion. Relevant discussion can also be found in (*16*). Maximum

burial depth of the Huqf-Haushi Outcrop Area can be estimated a variety of ways. The Huqf-Haushi Outcrop Area is interpreted as an area dominated by long term uplift surrounded by the down faulted Masirah Trough and the subsiding Ghaba Salt Basin (*133, 134*). The Huqf Supergroup in the Huqf-Haushi Outcrop Area has large-scale folds trending WSW-ENE to NNE-SSW (*133*). These folds result in the Khufai Formation preserved in outcrop as a series of steeply dipping (45° or less) anticlines surrounded by shallowing dipping Shuram and Buah Formation synclines. The gently dipping to flat lying Ordovician Mahatta Humaid Formation and Upper Carboniferous/Lower Permian Haushi Group onlap the outcrops of the Huqf Supergroup. Both the Ordovician and late Paleozoic deposits display no structural folding suggesting the deformation and uplift occurred during or shortly after deposition of the Huqf Supergroup (*133, 135*). Clay mineralogies within the Shuram and Buah Formations include illite, illite-smectite complexes, smectite and kaolinite (*136*) which suggests the Huqf-Huashi Outcrop Area hasn't experienced the full smectite-to-illite transition (burial $<$3000 m). Based on the structural history of the Huqf-Haushi Outcrop Area, we interpret the KD and MD sections as the shallowest buried of all samples analyzed for clumped isotope thermometry from Oman (*16*). As a whole the organic material from the Neoproterozoic Huqf Supergroup across Southern and Central Oman preserves a range of molecular biomarkers and sits in the marginal to middle oil window, representing some of the least thermally altered sediments of this time interval (*137, 138*).

The importance of diffusive solid state reordering on the clumped isotope thermometer has been estimated using laboratory heating experiments and reaction models (*139–141*). Estimates for optical calcite and brachiopod calcite indicate 1% reordering would occur between 115-127°C if the sample were held at those temperatures for 10 Ma and 101-112°C for 100 Ma. To achieve 99% reordered calcite in 10 Ma the modeled temperature range is 163-174°C or 144-155°C in 100 Ma (*141*). Evidence from blocking temperatures derived from marbles

indicates dolomite will be much less susceptible to solid state reordering (*139, 142*). Dolomite marbles yield blocking temperatures of $\sim$300°C whereas calcite marbles yield temperatures ranging from 150-200°C (*139, 143*). If a stratigraphic section reached temperatures able to drive diffusive reordering in calcite but not dolomite, we expect the calcitic samples to yield consistently higher temperatures and calculated ^{18}O-rich compositions for the fluid. Instead, calcitic samples from the recovery in the upper Shuram Formation yield similar temperatures to the pre-excursion upper Khufai Formation. Samples from the uppermost dolomites of the Khufai Formation yield similar temperatures and fluid oxygen isotope compositions to calcites from the lower and middle Shuram Formation. The combined estimates for minimal burial history from organic preservation and mineralogical similarities between calcite and dolomite suggest diffusive solid state reordering is not a significant process in these rocks (*16*).

Apatite thermochronology has similar to lower temperature sensitivities as calcite clumped isotope solid state re-ordering does for 100 Ma timescales and provides another point of comparison for maximum burial temperatures. Fission track ages from Huqf Supergroup detrital apatites, sourced from the 650-750 Ma granitic basement, range from 600 - 400 Ma with a peak at 450 Ma in wells from eastern Oman (*144*). This data suggests some wells never reached the apatite closure temperature of $\sim$100°C during burial and other wells experienced significant uplift around 450 Ma and saw maximum temperatures $<$100°Cfor the remainder of the Phanerozoic. Samples buried more deeply in the western part of Oman give more recent fission track ages indicating partial annealing (*144*).

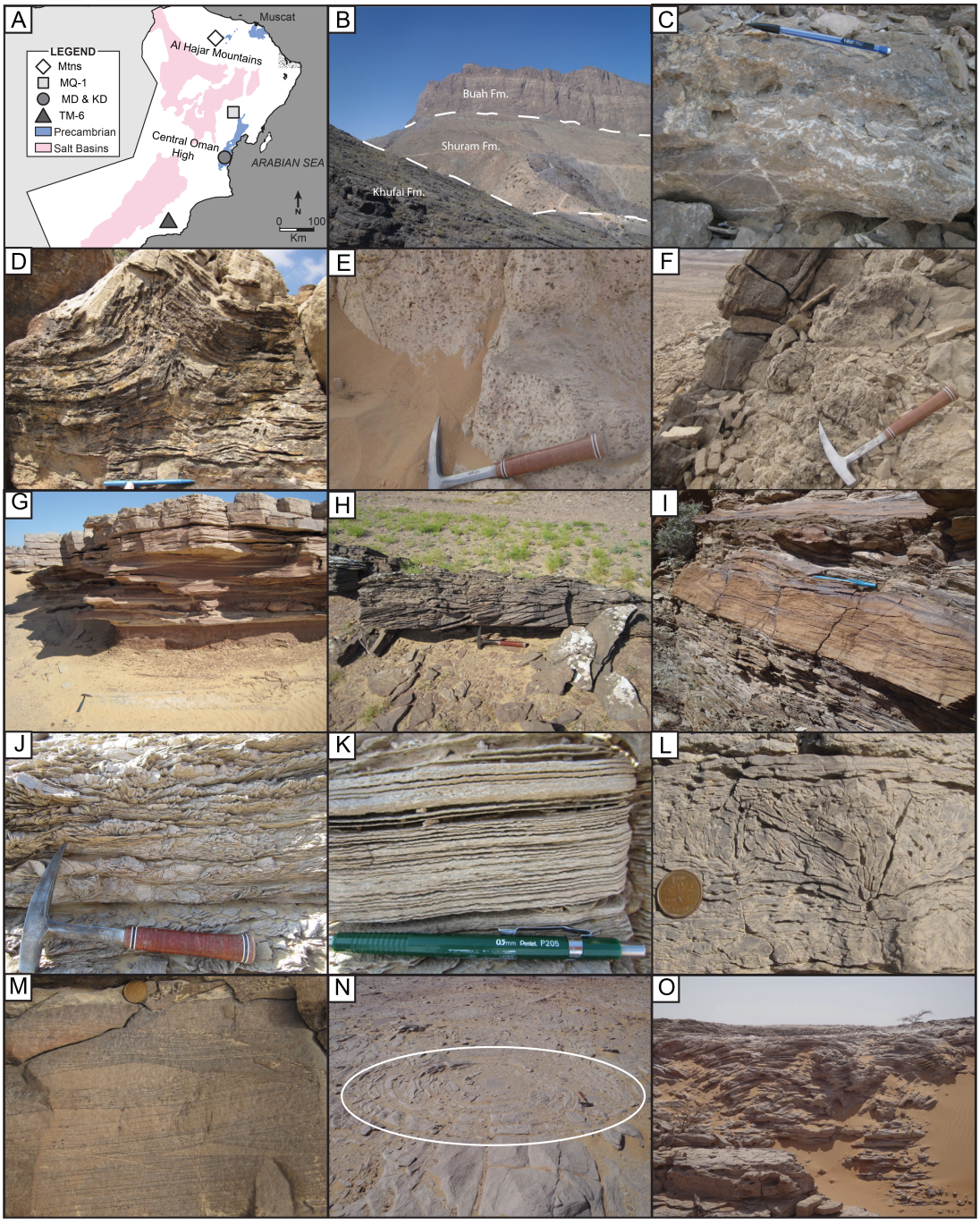

Fig. S1. Geologic context of the Shuram excursion. (**a**) Location map of the five stratigraphic sections analyzed. (**b**) Mountainside views of the three formations capturing the excursion in the Oman Mountains. (**c**) Diagenetic calcite from the Lower Khufai Formation. (**d, e**) Periti-

dal tepee and fenestral mudstone from the Upper Khufai Formation. (**f**) Transgressive systems tract recording the onset of the negative excursion in the Upper Khufai Formation. (**g, h**) Hummocky cross-stratified siltstones capped by ooid grainstones in the middle Shuram Formation. (**i**) Climbing ripples in the Shuram Formation from the Oman Mountains. (**j, k, l**), Edgewise conglomerate and crinkly laminite from the lower Buah Formation. (**m, n, o**) intraclast conglomerate and stromatolites bioherms from the Buah Formation.

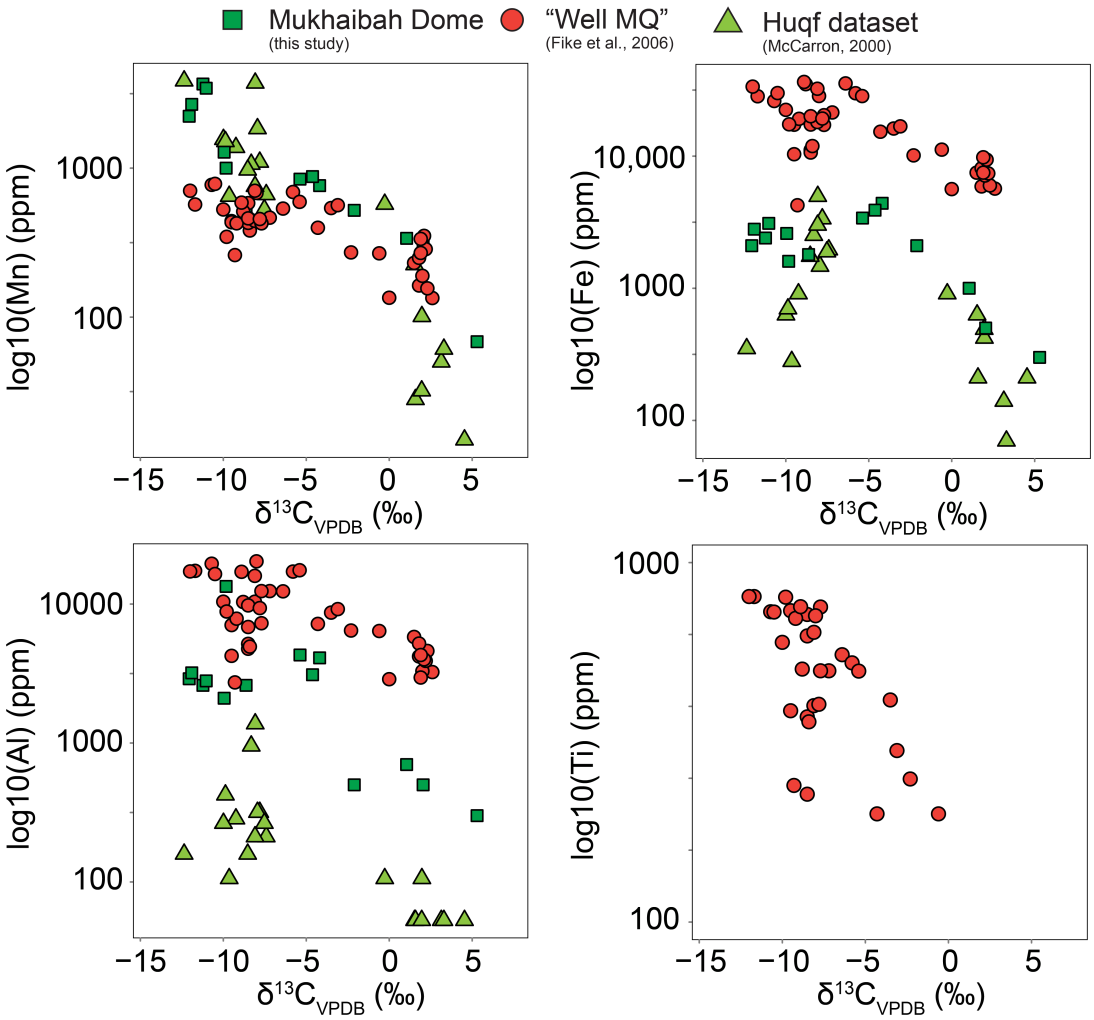

Fig. S2. Cross plots of bulk trace metal measurements versus δ^{13}C. a Log(Fe), log(Mn), log(Ti) and log(Al) versus δ^{13}C from three of the different sections analyzed. The magnitude of Fe, Al and Ti is higher for Well 'MQ' because that study dissolved well cuttings containing both siliciclastic and carbonate components in a strong acid as opposed to preferentially sampling carbonate. Data from this study and (*9, 145*).

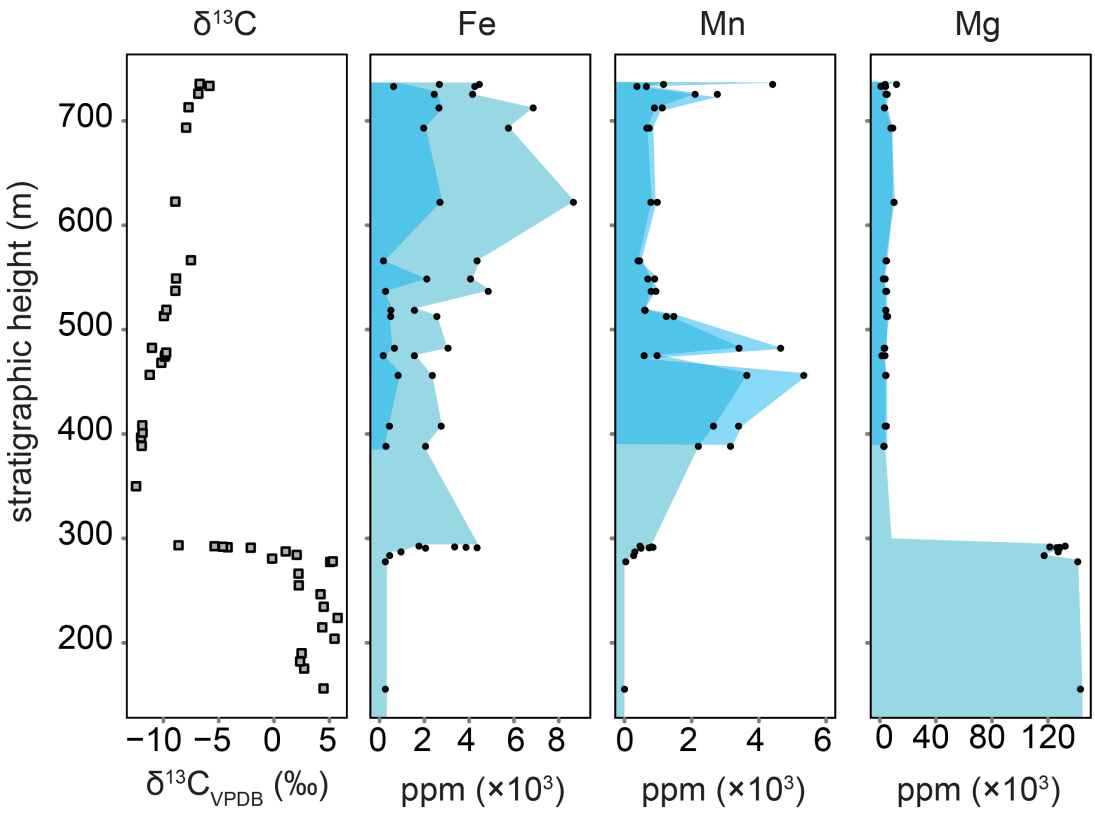

Fig. S3. Bulk strong acid (aqua regia) and acetic acid trace metal measurements from section MD for Fe, Mn and Mg. A strong acid dissolution (light blue) vs. an acetic acid dissolution (dark blue) targeting only the limestone indicates a significant component of the iron signal is not carried in the carbonate while most of the manganese signal is. The magnesium concentration confirms the observed mineralogical change to limestone.

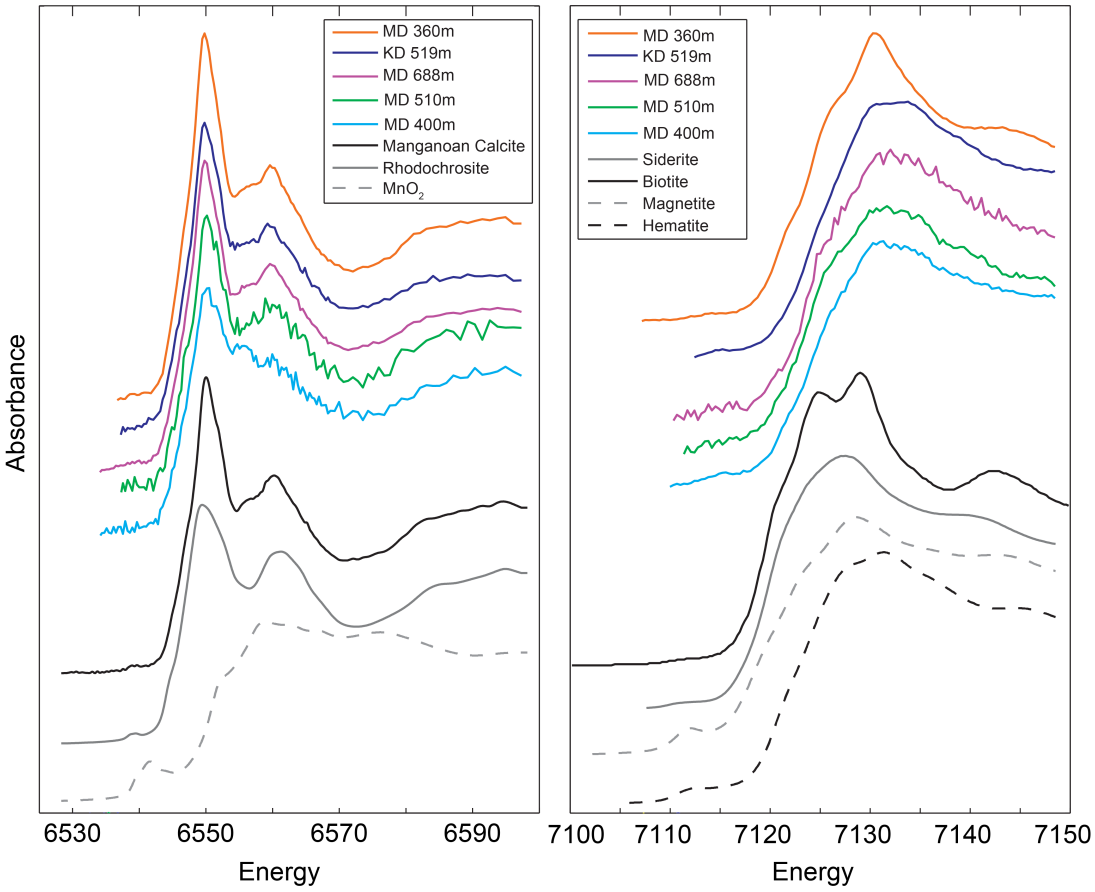

Fig. S4. Bulk XANES spectra of samples from the Shuram Formation. XANES spectra of samples from the nadir of the excursion yield consistent results indicating the iron is found in two phases hematite and biotite while the manganese is present as Mn(II) and most closely matches the spectra of manganoan calcite.

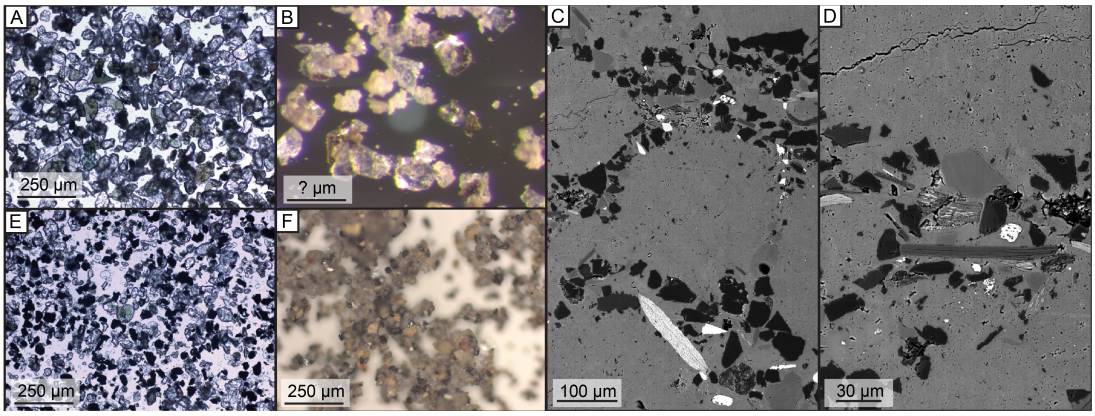

Fig. S5. Siliciclastic fraction of the Shuram (a–d) and Johnnie formations (e–f). (**a, e**) Wet grain mount under 10X magnification with visible biotite and muscovite grains. Iron oxides are more abundant in the sample from the Johnnie Formation. (**b, f**) Dry grain mount with quartz, muscovite, biotite, iron oxides and feldspars visible. The coarser grains from a fine-grained sandstone from the Shuram Formation include poorly weathered micas. (**c, d**) SEM images of iron-rich biotite grains within the detrital sediments filling in around the ooids.

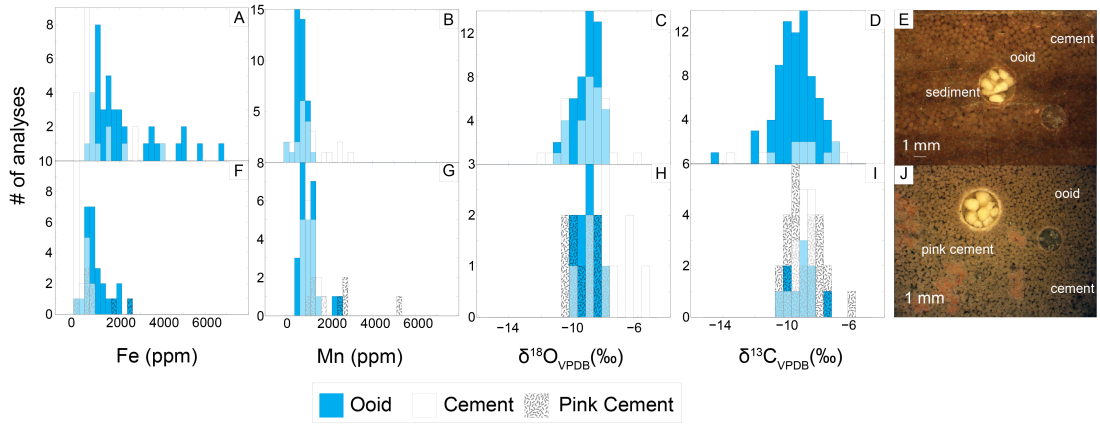

1242

1243 **Fig. S6. Histograms of in situ geochemical data for two samples from the Shuram Forma-**

1244 **tion. a, f** Spot analyses of iron (ppm) on ooids and two cement types—clear blocky cements

1245 and pink microcrystalline cements. **b, g** Spot analyses of manganese (ppm). **c, h** Spot analyses

1246 of $\delta^{13}C_{VPDB}$. d, i, spot analyses of $\delta^{18}O_{VPDB}$. **e, j** Images of each sample showing ooids, two

1247 types of cements and embedded standards (± 1‰ SD).

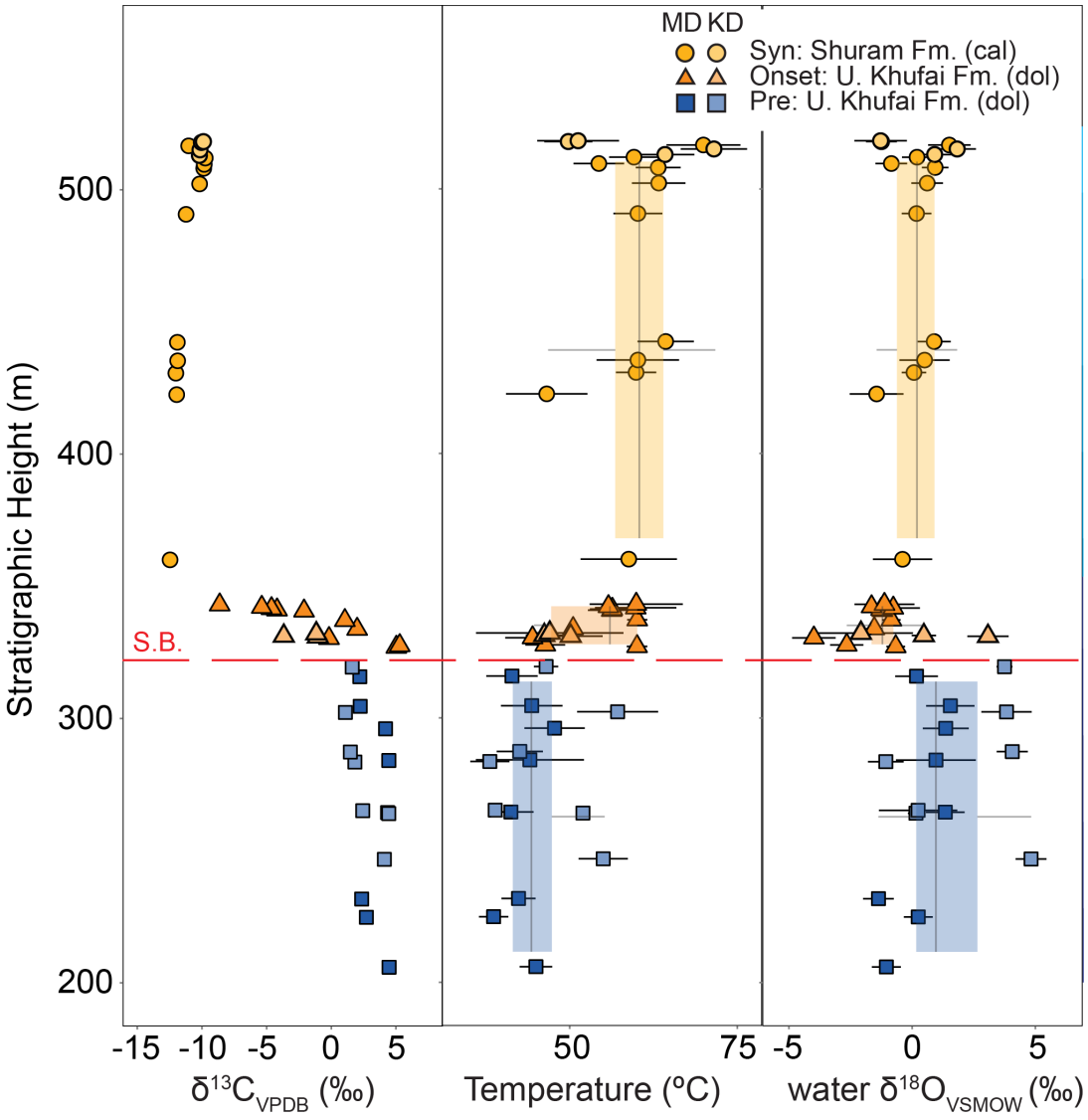

Fig. S7. Temperature and fluid oxygen isotope composition across the onset and nadir of the Shuram excursion. (**A**) Detailed stratigraphic section of the onset of the $\delta^{13}C_{VPDB}$ excursion with corresponding temperature and water $\delta^{18}O_{VSMOW}$ for MD and KD sections. Boxplots showing the minimum, maximum, standard deviation and mean for each population – pre-excursion, onset, and syn-excursion are also shown. The temperature change estimate from the modes of the density distributions of pre-excursion to syn-excursion populations are listed. Circles are calcite.

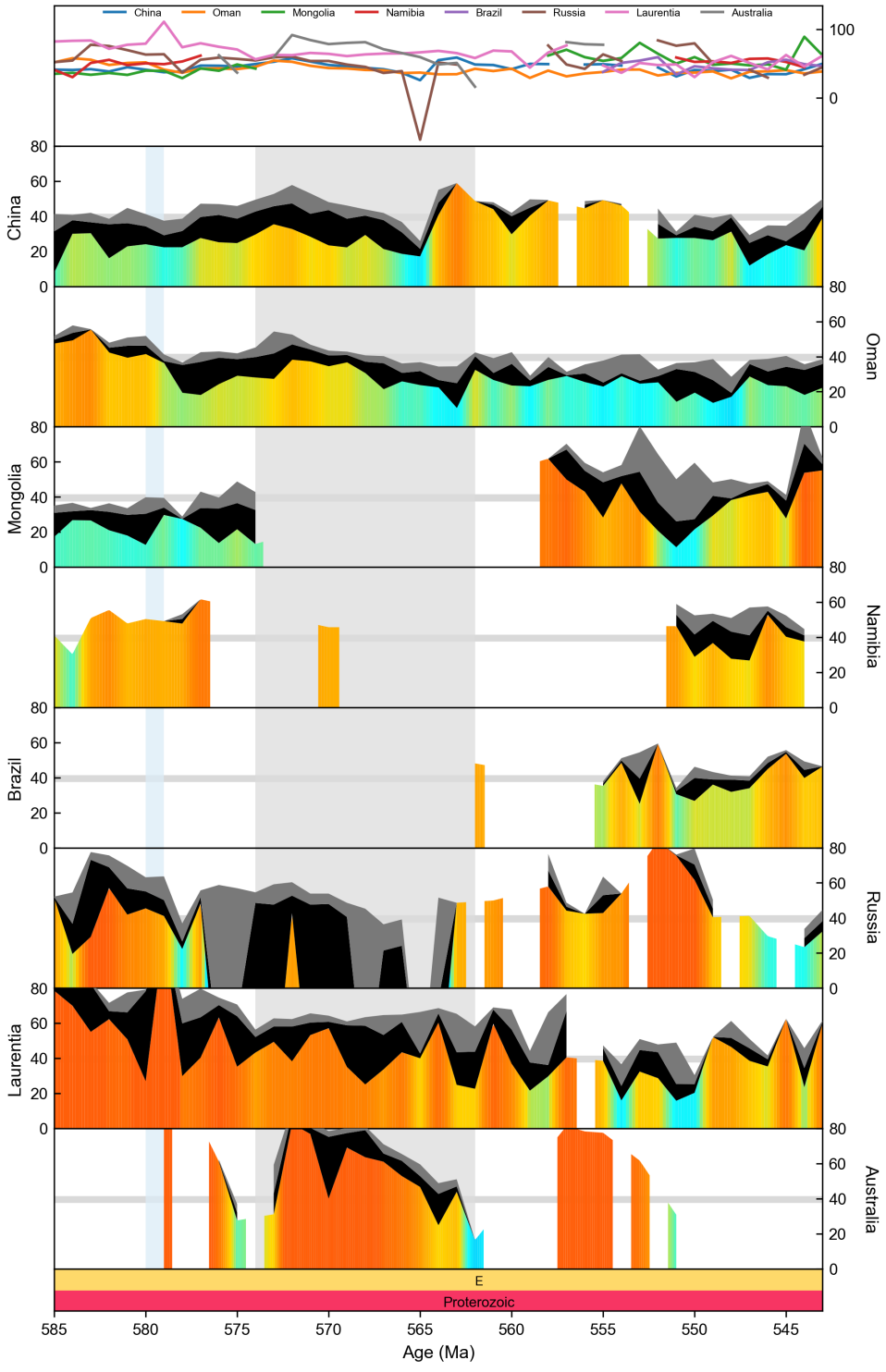

1256

1257 **Fig. S8. Ediacaran country-level contributions to the composite temperature record pre-**

sented in Fig. 5H. (**A**) Temperature comparison of the different countries. (**B-K**) The 1^{st} to 25^{th} quantiles (black) and 25th to 50th quantiles (grey) of shallow marine temperatures from Scenario 1 estimated using quantile regression on points within 1 Myr windows sampled each 1 Myr. In panel order, data are plotted from China, Oman, Mongolia, Namibia, Brazil, Russia, Laurentia (USA and Canada), and Australia. Grey bands represent the upper temperature limit of modern tropical subtidal ectotherms (*146*). Vertical bars indicate the Gaskiers glaciation (light blue) and the Shuram excursion (grey)

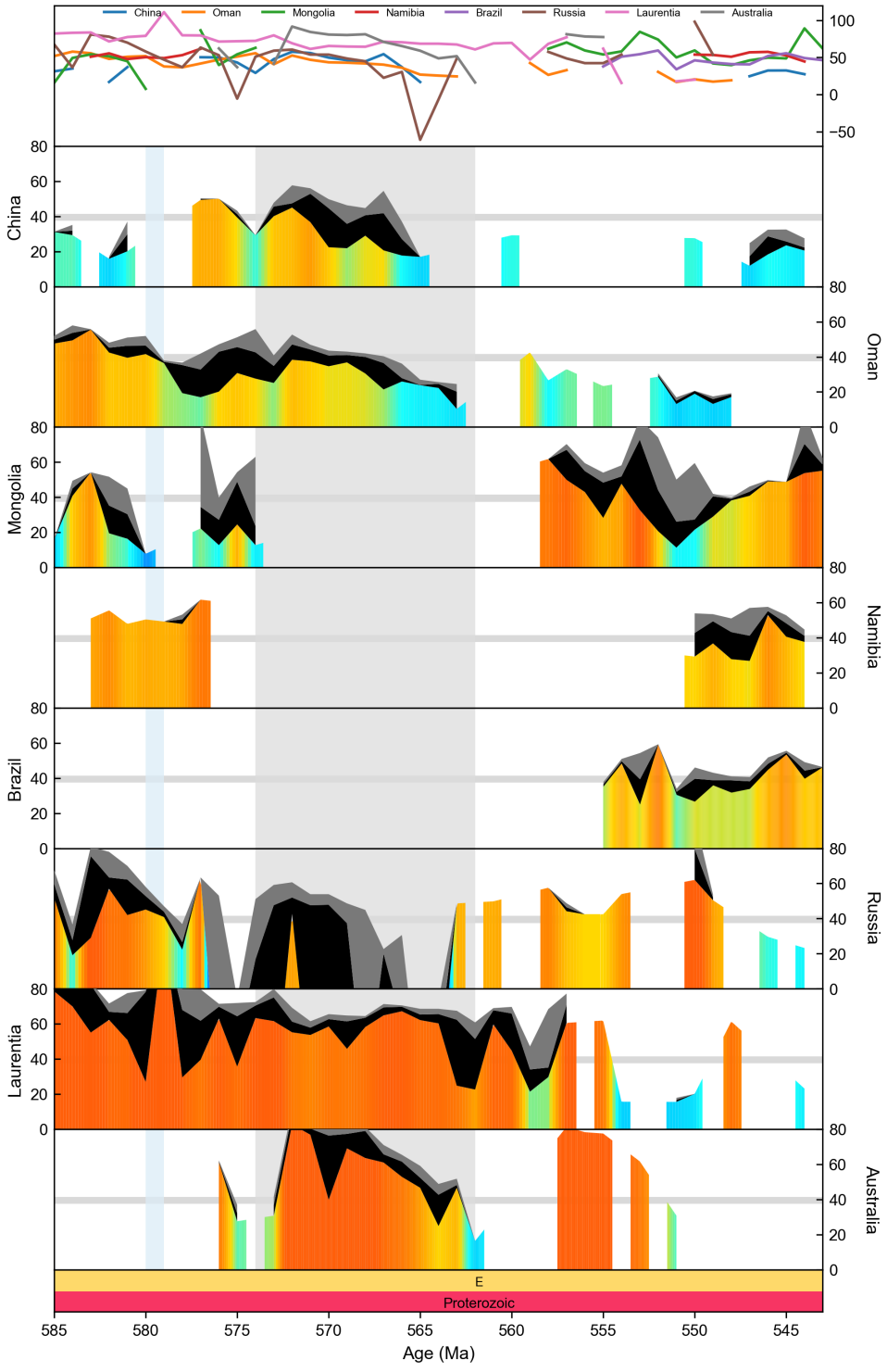

1266

1267 **Fig. S9. Ediacaran country-level contributions from limestone only to the composite tem-**

perature record presented in Fig. 5H. (**A**) Temperature comparison of the different countries. (**B-K**) The 1^{st} to 25$^{\text{th}}$ quantiles (black) and 25th to 50th quantiles (grey) of shallow marine temperatures from Scenario 1 estimated using quantile regression on points within 1 Myr windows sampled each 1 Myr. In panel order, data are plotted from China, Oman, Mongolia, Namibia, Brazil, Russia, Laurentia (USA and Canada), and Australia. Grey bands represent the upper temperature limit of modern tropical subtidal ectotherms (*146*). Vertical bars indicate the Gaskiers glaciation (light blue) and the Shuram excursion (grey)

Table. S1. Datasets from this manuscript Data from GPS, clumped isotope thermometry, XRD, bulk strong and weak acid trace metal analyses, SIMS, Electron microprobe and carbon and oxygen analyses.